Petroleum Science 23 (2026) 3248–3269

Contents lists available at ScienceDirect

Petroleum Science

journal homepage: www.keaipublishing.com/en/journals/petroleum-science

Original Paper

Phase-based polarized direct envelope inversion with total variation regularization for simultaneous source seismic data: Application to SEG 2014 Chevron blind test dataset

Yong Hu [a], Xi-Zhu Guan [b], Li-Yun Fu [c,*], Yi-Bo Wang [d], Ru-Shan Wu [e]

[a] School of Resources and Geosciences, China University of Mining and Technology, Xuzhou, 221116, Jiangsu, China
[b] CNOOC Research Institute Co., Ltd., Beijing, 100028, China
[c] State Key Laboratory of Deep Oil and Gas, China University of Petroleum (East China), Qingdao, 266580, Shandong, China
[d] Research Center for Oil-Gas Theories and Methods, Institute of Geology and Geophysics, Chinese Academy of Sciences, Beijing, 100029, China
[e] Department of Earth and Planetary Sciences, University of California at Santa Cruz, Santa Cruz, 95064, USA

ARTICLE INFO

Article history:
Received 7 August 2025
Received in revised form
19 December 2025
Accepted 8 April 2026
Available online 13 April 2026

Edited by Meng-Jiao Zhou

Keywords:
Full waveform inversion
Direct envelope inversion
Polarity envelope
Chevron blind dataset test
Total variation regularization

ABSTRACT

In subsalt hydrocarbon exploration, the strong velocity contrast associated with salt structures poses significant challenges to conventional full waveform inversion (FWI) method. While direct envelope inversion can invert large-scale salt dome, it fails to invert the salt-bottom velocity structures due to the absence of waveform phase information. To solve this problem, we first use a sliding Gaussian window to decompose seismic data into the local scale waveform. Subsequently, we combine the local scale envelope signal with waveform instantaneous phase to obtain the polarity envelope. The resulting polarity envelope can invert low-frequency components while preserving the phase characteristics of seismic data, enabling more accurate low-wavenumber velocity structures. Based on this, we propose a phase-based polarized direct envelope inversion with total variation regularization for simultaneous source seismic data (simultaneous source TV-PDEI) to improve the accuracy of velocity inversion, remove the crosstalk noise, and enhance the computational efficiency. Numerical experiments on salt models and Chevron blind dataset test demonstrate that the simultaneous source TV-PDEI efficiently provides a robust initial velocity model for FWI.

1. Introduction

Large-scale and strong-contrast salt structures can form significant hydrocarbon traps in surrounding sediments (Ramirez et al., 2016). Following the discovery of sub-salt oil and gas fields in Kuqa, Xinjiang, research into inversion and imaging of salt dome structures has shown tremendous economic potential in China's oil and gas exploration. Recent advancements in computational technology have enabled high-resolution, computationally-intensive methods like full waveform inversion (FWI) to make significant progress. FWI leverages the dynamic and kinematic characteristics of seismic waves to yield high-resolution inversion results (Lailly, 1983; Tarantola, 1984). However, FWI relies on the Born approximation assumption, which poses challenges in accurately inverting large-scale strong-contrast salt dome structures (Kadu et al., 2016; Kalita et al., 2019; Chen et al., 2018).

The low-frequency components of seismic data are crucial for capturing low-wavenumber information of velocity structures, particularly in inverting strong-contrast salt structures. However, acquiring high signal-to-noise ratio seismic signals below 4 Hz is challenging, leading to severe cycle-skipping issues in FWI. Fortunately, the envelope of seismic data contains abundant low-frequency components, which can aid in recovering a reliable initial velocity model for FWI. Fichtner et al. (2008) used amplitude spectrum in the time-frequency domain as the energy envelope and tested differences between envelope and phase inversion. Following this, Bozdağ et al. (2011) employed Hilbert transform analysis to extract envelope signals, leading to envelope inversion testing. Most subsequent envelope inversion methods have been built on the Hilbert transform, such as those by Wu et al. (2014) and Chi et al. (2014), who pointed out that envelope signals rich in low-frequency components effectively compensate for

* Corresponding author.
E-mail address: lfu@upc.edu.cn (L.-Y. Fu).
Peer review under the responsibility of China University of Petroleum (Beijing).

https://doi.org/10.1016/j.petsci.2026.04.013

missing low-frequency seismic data, assisting the reconstruction of low-wavenumber velocity structures. Numerical tests affirm the advantages of envelope inversion in initial velocity model building. Luo and Wu (2015) analyzed the noise resistance advantages of envelope inversion. Ao et al. (2015) explored the source-independent envelope inversion, suggesting the convolution of reference traces with data to calculate the envelope, thus achieving independence from the source wavelet while maximizing the low-frequency advantage of envelopes. Hu et al. (2017) identified instability issues with envelope-related adjoint sources at near offsets and proposed a demodulated envelope inversion method that better utilizes low-frequency advantages for velocity model low-wavenumber components. However, traditional envelope inversion assumes weak scattering and struggles with large-scale strong-contrast salt velocity model building.

To overcome the limitations of the weak scattering assumption and address the velocity inversion problem for large-scale strong scattering structures like salt domes, direct envelope inversion (DEI) has been introduced (Wu and Chen, 2017; Zhang et al., 2018; Chen et al., 2018). Within the theoretical framework of DEI, Wang et al. (2018) incorporated positive and negative polarity information into envelope signals, improving inversion results. Hu et al. (2019) improved the resolution of salt-bottom and subsalt velocity inversion by utilizing amplitude and phase misfit functions in the time-frequency domain of envelope signals. However, the envelope signal loses the original phase information of seismic data, impacting salt-bottom velocity structures building. Hu et al. (2022) integrated instantaneous phase information into envelope signals, proposing the polarized direct envelope inversion, significantly improving the resolution of salt-bottom. Lee et al. (2024) addressed computational intensity issues in DEI by introducing excitation amplitude and time strategies, demonstrating improved computational efficiency through numerical testing. Although polarity envelope inversion effectively addresses the subsalt and salt-bottom velocity inversion, the modification of original seismic waveforms and the introduction of noise can impact the stability of the inversion results.

Regularization methods play a pivotal role in seismic inversion by addressing issues of non-uniqueness and oscillatory solutions, thereby ensuring stable convergence and enhancing noise resistance towards the minimum of the misfit function (Tikhonov and Arsenin, 1977). Given the strong nonlinearity inherent in full waveform inversion (FWI), the incorporation of regularization techniques significantly bolsters inversion stability. For instance, Burstedde and Ghattas (2009) explored Tikhonov and total variation regularizations, demonstrating that FWI constrained by total variation effectively inverts large-scale blocky geological structures, such as salt domes. This approach provides valuable insights into constructing strong-contrast velocity models (Yong et al., 2018; Kalita et al., 2019). To mitigate the influence of noise on inversion results, Li et al. (2012) successfully applied sparse regularization to FWI, achieving clearer subsurface structural inversion results. Subsequent studies have verified that, although velocity models are typically sparse-deficient, sparse transformations such as wavelet transform, curvelet transform, and dictionary learning can induce sparsity in subsurface velocity models. Integrating these transformations into the FWI workflow obtains more stable inversion results (Zhu et al., 2015). Feng et al. (2019) enhanced inversion resolution and computational efficiency by employing wavefield reconstruction inversion along with total variation regularization on Ground Penetrating Radar data. Fu et al. (2021) advanced FWI using adaptive complete dictionary learning, successfully preserving model detail while suppressing noise. Yang and Ma (2023) combined optimal transport FWI with deep learning and incorporated regularization constraints, demonstrating significant advantages in inverting complex, strong-contrast salt domes. Song et al. (2024) introduced the source wavelet as a regularization term in elastic wavefield reconstruction inversion, achieving improved waveform matching and resolution in complex structures. Thus, regularization constraints are vital in enhancing the stability and noise resistance of seismic inversion methods.

In this study, based on direct envelope inversion, we propose a Phase-based polarized direct envelope inversion with total variation regularization for simultaneous source seismic data (simultaneous source TV-PDEI) method to address algorithmic stability issues in salt velocity model building, providing a reliable initial velocity model for FWI. We first describe the integrated instantaneous phase information into envelope signals to construct a polarity envelope. Subsequently, we introduce the misfit function for PDEI and its adjoint source. We then detail the simultaneous source TV-PDEI and derive the gradient operator. Finally, numerical testing using salt models and Chevron blind dataset test evaluates the advantages of simultaneous source TV-PDEI in velocity model inversion.

2. Theory

2.1. Direct envelope inversion

Envelope signals contain abundant low-frequency components, which are advantageous for velocity model building in media with strong contrasts. However, conventional envelope inversion, based on the Born approximation theory, fails to transmit most of these low-frequency components to the adjoint sources, thereby limiting its capability to invert structures like strong-contrast salt domes. To address this limitation, Wu and Chen (2017) proposed the Direct Envelope Inversion (DEI) method. The DEI misfit function can be expressed as:

$$J_{\mathrm{E}}(\mathbf{v}) = \frac{1}{2}\sum_{Ns}\sum_{Nt}\sum_{Nr}\left[E_{\mathrm{u}}(t) - E_{\mathrm{d}}(t)\right]^2 , \tag{1}$$

where $E_{\mathrm{u}}(t)$ denotes the envelope of the synthetic data, and $E_{\mathrm{d}}(t)$ represents the envelope of the observed data. The parameter $\mathbf{v}$ represents the velocity model; Ns stands for the number of sources; Nr signifies the number of receivers per shot; Nt is the number of time samples. To update the velocity model, we calculate the partial derivative of the misfit function with respect to the velocity parameter, expressed as:

$$\frac{\partial J_{\mathrm{E}}(\mathbf{v})}{\partial \mathbf{v}} = \sum_{Ns}\sum_{Nt}\frac{\partial (E_{\mathrm{u}})}{\partial \mathbf{v}} \quad (E_{\mathrm{u}} - E_{\mathrm{d}}), \tag{2}$$

where $\mathbf{F}_{\mathrm{E}} = \partial E_{\mathrm{u}}/\partial \mathbf{v}$ is the Fréchet derivative of the direct envelope (Wu and Chen, 2017; Chen et al., 2018; Zhang et al., 2018; Hu et al., 2022). The gradient of DEI is then expressed as:

$$\frac{\partial J_{\mathrm{E}}(\mathbf{v})}{\partial \mathbf{v}} = \frac{1}{\mathbf{v}_0}\sum_{Ns}\sum_{Nt}\left(P_{\mathrm{f}}^{\mathrm{E}}\right)\left(P_{\mathrm{b}}^{\mathrm{E}}\right), \tag{3}$$

where $P_{\mathrm{f}}^{\mathrm{E}}$ is the envelope of the forward-propagated wavefield, and $P_{\mathrm{b}}^{\mathrm{E}}$ is the back-propagated wavefield of energy residual. For more detail about DEI gradient, please refer to Appendices A, B, and C.

2.2. Construction of polarity envelope

Seismic envelope signals, characterized by a richness in low-frequency components, unfortunately lack the phase information inherent in original seismic data. This deficit can lead to inaccuracies in constructing velocity models, particularly at the salt-bottom, when employing the DEI method. To mitigate this challenge, we propose an integration of the instantaneous phase information from seismic data with the envelope signal to develop a polarity envelope. This innovative approach aims to preserve the phase detail of seismic data while harnessing the low-frequency richness of the envelope signal. In constructing the polarity envelope, we first use a sliding Gaussian window to extract the local-scale waveform information from the seismic data, expressed as:

$$u(\tau,t) = u(t)\ h(t-\tau), \tag{4}$$

where $h(t)$ represents the Gaussian window; The single trace waveform and the local-scale seismic data are illustrated in Fig. 1(a) and (b), respectively. Next, we compute the envelope of the localized seismic data as follows:

$$E_u(\tau,t) = \sqrt{\{\ u(\tau,t)\ \}^2 + \{\ \mathbf{H}\,[u(\tau,t)\ ]\ \}^2} \tag{5}$$

where $\mathbf{H}\,[\ \cdot\ ]$ denotes the Hilbert transform operator, and $E_u(\tau,t)$ represents the envelope in the local-scale domain, as shown in Fig. 1(c).

By combining the 2D local-scale seismic data with its envelope, we identify the time coordinate of the maximum envelope value within each window function:

$$T(\tau) = \underset{t}{\operatorname{argmax}}[\ E_u(\tau,t)\ ]. \tag{6}$$

Next, we calculate instantaneous phase of seismic waveforms at $T(\tau)$. The instantaneous phase can be expressed as:

$$\alpha_u(\tau) = \mathrm{Im}\left\{\ln\left(\frac{\tilde{u}(\tau,T(\tau))}{E_u(\tau,T(\tau))}\right)\right\}, \tag{7}$$

where $\tilde{u}\ = u + j\,\mathbf{H}\,[u]$. Next, the polarity envelope can be calculated with the instantaneous phase and the envelope signal using the phase rotation formula:

$$E_{\mathrm{pu}}(\tau,t) = E_u(\tau,t)\cos(\alpha_u(\tau)\ ) - \mathbf{H}\,[E_u(\tau,t)\ ]\sin(\alpha_u(\tau)\ ), \tag{8}$$

where $E_{\mathrm{pu}}(\tau,t)$ represents the polarity envelope in the local-scale domain. This combination of envelope signal and waveform phases, allowing us to capture both the phase information and the low-frequency content of the seismic data. By inverse transforming the local-scale polarity envelope back to the time domain, we obtain the final polarity envelope signal. The inverse transformation of polarity envelope can be expressed as:

$$E_{\mathrm{pu}}(t) = \int_R E_{\mathrm{pu}}(\tau,t)\ h(t-\tau)\ \mathrm{d}\tau, \tag{9}$$

where $E_{\mathrm{pu}}(t)$ is the polarity envelope of a single seismic trace. For a single shot record, it can be done trace by trace. Fig. 2 demonstrates a seismic trace along with its envelope and polarity envelope waveform. It shows different results for polarity envelopes with varying window lengths: larger windows produce smoother waveforms with richer low-frequency components, while shorter windows yield waveforms closer to the original seismic data. This observation suggests a multiscale inversion strategy, starting with

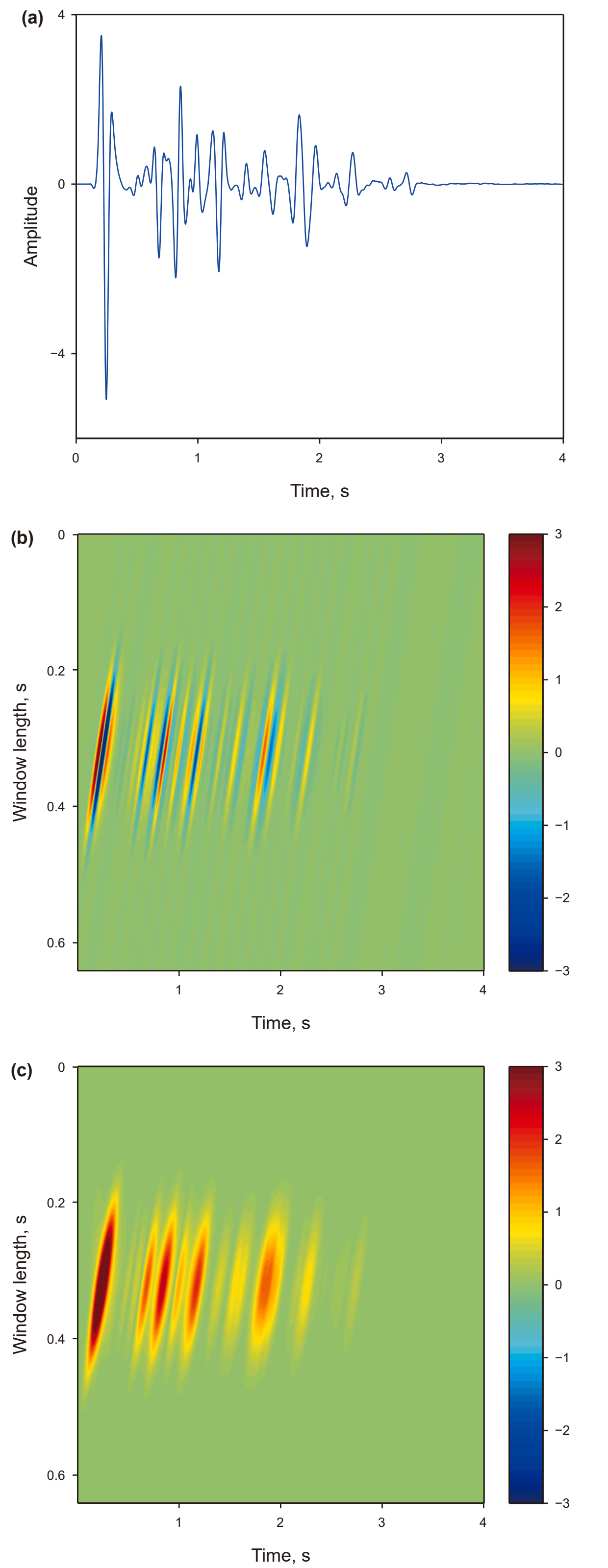

Fig. 1. Single trace seismic data and its local-scale transform, **(a)** single trace waveform; **(b)** 2D local-scale seismic data; **(c)** 2D local-scale envelope.

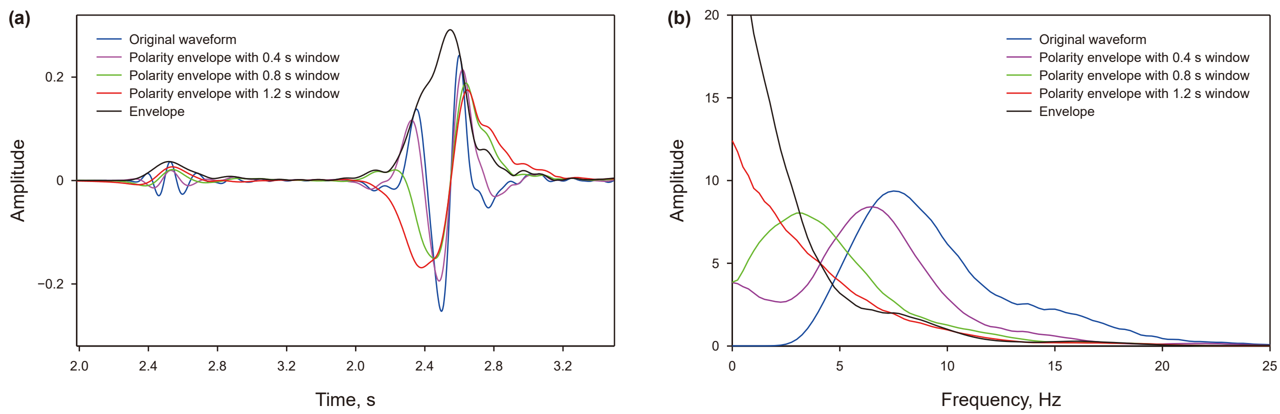

Fig. 2. Comparison of seismic waveform, envelope, and polarity envelope, **(a)** waveform comparison; **(b)** spectrum.

larger windows for PDEI and progressively reducing the window length to transition from low wavenumber to high wavenumber inversion. The original seismic data in Fig. 2 lacks frequencies below 4 Hz, whereas the polarity envelope signal exhibits abundant low-frequency component while preserving the original seismic data's oscillatory trends (including phase information). This demonstration validates the effectiveness of the local-scale-based polarity envelope construction method.

2.3. Simultaneous source based polarized direct envelope inversion

To further enhance the computational efficiency of PDEI, we incorporate a simultaneous source encoding strategy into the PDEI misfit function. It is formulated as:

$$J_{\mathrm{SPE}}(\mathbf{v}) = \frac{1}{2}\sum_{Ns}\sum_{Nt}\sum_{Nr}\left[E_{\mathrm{spu}}(t) - E_{\mathrm{spd}}(t)\right]^2 \tag{10}$$

where $E_{\mathrm{spu}}(t)$ represents the polarity envelope of the synthetic simultaneous source seismic data, and $E_{\mathrm{spd}}(t)$ denotes the envelope of the observed simultaneous source seismic data. To obtain updates to the velocity model, we derive the partial derivative of the misfit function concerning the velocity parameter, expressed as:

$$\frac{\partial J_{\mathrm{SPE}}(\mathbf{v})}{\partial \mathbf{v}} = \sum_{Ns}\sum_{Nt}\frac{\partial (E_{\mathrm{spu}})}{\partial \mathbf{v}}\left(E_{\mathrm{spu}} - E_{\mathrm{spd}}\right), \tag{11}$$

where $\partial E_{\mathrm{spu}}/\partial \mathbf{v}$ is the Fréchet derivative of the polarity envelope of the synthetic simultaneous source seismic data. Consequently, the gradient of simultaneous source PDEI is given by:

$$\frac{\partial J_{\mathrm{SPE}}(\mathbf{v})}{\partial \mathbf{v}} = \frac{1}{\mathbf{v}_0}\sum_{Ns}\sum_{Nt}\left(P_{\mathrm{f}}^{\mathrm{SPE}}\right)\left(P_{\mathrm{b}}^{\mathrm{SPE}}\right) \tag{12}$$

where $P_{\mathrm{f}}^{\mathrm{SPE}}$ is the envelope of the forward-propagated wavefield, and $P_{\mathrm{b}}^{\mathrm{SPE}}$ is the envelope residual back-propagated wavefield. The corresponding adjoint source can thereby be defined as $R^{\mathrm{SPDEI}} = E_{\mathrm{spu}} - E_{\mathrm{spd}}$.

2.4. Simultaneous source-based polarized direct envelope inversion with total variation regularization

To address the challenges of stability and cross-talk noise inherent in the simultaneous source PDEI, we integrate a total variation (TV) regularization approach, resulting in the Phase-based polarized direct envelope inversion with total variation regularization (simultaneous source TV-PDEI) method. The misfit function can be expressed as:

$$J_{\mathrm{SPE-TV}}(\mathbf{v}) = \frac{1}{2}\sum_{Ns}\sum_{Nt}\sum_{Nr}\left[E_{\mathrm{spu}}(t) - E_{\mathrm{spd}}(t)\right]^2 + \eta\,\lambda_{\mathrm{TV}}\,\|\,\mathbf{v}\,\|_{\mathrm{TV}} \tag{13}$$

where λ_{TV} regulates the weight between the data fidelity term and the model constraint term. The total variation regularization can be defined as:

$$J_{\mathrm{TV}}(\mathbf{v}) = \|\mathbf{v}\|_{\mathrm{TV}} = \int_{\Omega}\sqrt{\beta + \mathbf{v}_x^2 + \mathbf{v}_z^2}\,\mathrm{d}x\mathrm{d}z \tag{14}$$

In the simultaneous source TV-PDEI misfit function, it is essential to normalize the gradients of both data and model constraints, necessitating the introduction of another weighting factor $\eta = \max(|\mathbf{g}_{\mathrm{data}}|)/\max(|\mathbf{g}_{\mathrm{TV}}|)$, where $\mathbf{g}_{\mathrm{data}}$ represents the gradient of the data constraint, and $\mathbf{g}_{\mathrm{TV}}$ denotes the gradient of the model constraint. The partial derivative of the misfit function with respect to the velocity parameter is expressed as:

$$\begin{aligned}\frac{\partial J_{\mathrm{SPE-TV}}(\mathbf{v})}{\partial \mathbf{v}} = &\sum_{Ns}\sum_{Nt}\frac{\partial (E_{\mathrm{spu}})}{\partial \mathbf{v}}\left(E_{\mathrm{spu}} - E_{\mathrm{spd}}\right)\\ &+ \eta\,\lambda_{\mathrm{TV}}\frac{\partial}{\partial \mathbf{v}}\left(\int_{\Omega}\sqrt{\beta + \mathbf{v}_x^2 + \mathbf{v}_z^2}\,\mathrm{d}x\mathrm{d}z\right)\end{aligned} \tag{15}$$

where $\mathbf{v}_x = \partial \mathbf{v}/\partial x$, $\mathbf{v}_z = \partial \mathbf{v}/\partial z$, β is a small positive number used to avoid division by zero. The partial derivative of the model constraint term with respect to the velocity parameter is:

$$\begin{aligned}\frac{\partial J_{\mathrm{TV}}(\mathbf{v})}{\partial \mathbf{v}} &= -\frac{\partial}{\partial x}\left(\frac{\partial\sqrt{\beta+\mathbf{v}_x^2+\mathbf{v}_z^2}}{\partial \mathbf{v}_x}\right)-\frac{\partial}{\partial z}\left(\frac{\partial\sqrt{\beta+\mathbf{v}_x^2+\mathbf{v}_z^2}}{\partial \mathbf{v}_z}\right)\\ &= -\left[\frac{\partial}{\partial x}\left(\frac{\mathbf{v}_x}{\sqrt{\beta+\mathbf{v}_x^2+\mathbf{v}_z^2}}\right)+\frac{\partial}{\partial z}\left(\frac{\mathbf{v}_z}{\sqrt{\beta+\mathbf{v}_x^2+\mathbf{v}_z^2}}\right)\right]\\ &= -\left\{\frac{\left[\mathbf{v}_{xx}\sqrt{\beta+\mathbf{v}_x^2+\mathbf{v}_z^2}-\frac{\mathbf{v}_x(2\mathbf{v}_x\mathbf{v}_{xx}+2\mathbf{v}_z\mathbf{v}_{zx})}{2\sqrt{\beta+\mathbf{v}_x^2+\mathbf{v}_z^2}}\right]}{\left(\beta+\mathbf{v}_x^2+\mathbf{v}_z^2\right)}\right.\\ &\qquad\left.+\frac{\left[\mathbf{v}_{zz}\sqrt{\beta+\mathbf{v}_x^2+\mathbf{v}_z^2}-\frac{\mathbf{v}_z(2\mathbf{v}_x\mathbf{v}_{xz}+2\mathbf{v}_z\mathbf{v}_{zz})}{2\sqrt{\beta+\mathbf{v}_x^2+\mathbf{v}_z^2}}\right]}{\left(\beta+\mathbf{v}_x^2+\mathbf{v}_z^2\right)}\right\}\\ &= -\frac{\mathbf{v}_{xx}\left(\mathbf{v}_z^2\right)+\mathbf{v}_{zz}\left(\mathbf{v}_x^2\right)-2\mathbf{v}_x\mathbf{v}_z\mathbf{v}_{xz}+\beta\left(\mathbf{v}_{xx}+\mathbf{v}_{zz}\right)}{\left(\beta+\mathbf{v}_x^2+\mathbf{v}_z^2\right)^{\frac{3}{2}}}\end{aligned} \tag{16}$$

where $\mathbf{v}_{xx}=\partial^2\mathbf{v}/\partial x^2$, $\mathbf{v}_{zz}=\partial^2\mathbf{v}/\partial z^2$, $\mathbf{v}_{xz}=(\partial/\partial x)(\partial\mathbf{v}/\partial z)$ represent differentiation operators in the x and z directions. The corresponding finite difference scheme is:

$$\begin{cases}\mathbf{v}_x^{i,j}=\dfrac{\mathbf{v}^{i+1,j}-\mathbf{v}^{i,j}}{\Delta x}\\ \mathbf{v}_z^{i,j}=\dfrac{\mathbf{v}^{i,j+1}-\mathbf{v}^{i,j}}{\Delta z}\\ \mathbf{v}_{xx}^{i,j}=\dfrac{\mathbf{v}^{i+1,j}-2\mathbf{v}^{i,j}+\mathbf{v}^{i-1,j}}{(\Delta x)^2}\\ \mathbf{v}_{zz}^{i,j}=\dfrac{\mathbf{v}^{i,j+1}-2\mathbf{v}^{i,j}+\mathbf{v}^{i,j-1}}{(\Delta z)^2}\\ \mathbf{v}_{xz}^{i,j}=\dfrac{\mathbf{v}^{i+1,j+1}+\mathbf{v}^{i-1,j-1}-\mathbf{v}^{i+1,j-1}+\mathbf{v}^{i-1,j+1}}{4\Delta x\Delta z}\end{cases} \tag{17}$$

Finally, the gradient of the misfit function with respect to the velocity parameter is:

$$\begin{aligned}\frac{\partial J_{\mathrm{SPE-TV}}(\mathbf{v})}{\partial \mathbf{v}} &= \frac{1}{\mathbf{v}_0}\sum_{Ns}\sum_{Nt}\left(P_{\mathrm{f}}^{\mathrm{SPE}}\right)\left(P_{\mathrm{b}}^{\mathrm{SPE}}\right)\\ &\quad-\eta\,\lambda_{\mathrm{TV}}\left[\frac{\mathbf{v}_{xx}\left(\mathbf{v}_z^2\right)+\mathbf{v}_{zz}\left(\mathbf{v}_x^2\right)-2\mathbf{v}_x\mathbf{v}_z\mathbf{v}_{xz}+\beta\left(\mathbf{v}_{xx}+\mathbf{v}_{zz}\right)}{\left(\beta+\mathbf{v}_x^2+\mathbf{v}_z^2\right)^{\frac{3}{2}}}\right]\end{aligned} \tag{18}$$

Therefore, the update to the velocity model can be obtained for the simultaneous source TV-PDEI method, balancing the polarity envelope data fidelity with spatial smoothness constraints to mitigate noise and improve stability in strong-contrast media model building.

3. Numerical examples

3.1. Salt model gradients and adjoint sources analysis

In this section, we use synthetic data from a salt model to assess the inversion performance of several methods: FWI, DEI, PDEI, TV-PDEI, and simultaneous source TV-PDEI. The true salt velocity model is illustrated in Fig. 3(a), and the initial velocity model is depicted in Fig. 3(b). Notably, the initial model does not contain any salt structures and shows a significant velocity contrast, posing a considerable challenge for FWI. The dimensions of the salt model are 7 km in horizontal distance and 1.75 km in vertical depth, with a grid spacing of 25 m. There are 60 sources placed on the surface, each corresponding to 280 receivers. A Ricker wavelet with a dominant frequency of 8 Hz is used as the source wavelet. The maximum recording time is 4 s, with a time sampling interval of 2 ms. To realistically simulate the loss of low-frequency data typical in field acquisitions, frequencies below 4 Hz are filtered out of the seismic data.

To better understand the differences between FWI, DEI, and PDEI, this section provides a detailed analysis of the adjoint sources and gradients for these three methods. Fig. 4 presents a comparative analysis of the adjoint sources derived from each method, from which the following observations can be made: (1) FWI adjoint source: The waveforms exhibit significant oscillations, indicating that the dominant frequency is relatively high. This characteristic is not conducive to recovering the low wavenumber components crucial for accurately recovering strong-contrast velocity structures like salt domes; (2) DEI adjoint source: The waveforms change more smoothly, suggesting a lower dominant frequency with a rich presence of low-frequency components. This is beneficial for capturing the low wavenumber components of strong-contrast structures. However, the waveform phase information in the region indicated by the arrow is reversed compared to the FWI adjoint source. This phase discrepancy causes inaccuracies in inverting the velocity at the salt-bottom when using the DEI method; (3) PDEI adjoint source: Similar to DEI adjoint source, PDEI adjoint source retains abundant low-frequency content to effectively invert the low wavenumber features of strong-contrast velocity models. However, unlike DEI adjoint source, the waveform phase in the arrow-indicated region aligns with that of the FWI adjoint source. This alignment demonstrates that PDEI adjoint source preserves the seismic data's phase information well, thus avoiding inaccuracies in recovering the salt-bottom boundaries. Nevertheless, the PDEI adjoint source contains noticeable vertical stripe noise, primarily due to issues in constructing the polarity envelope, which can be suppressed with multiple shot stacking. Although such noise can be reduced through multiple shot stacking, it becomes more pronounced in simultaneous source, potentially affecting inversion precision. Thus, employing regularization methods is crucial to alleviate the impact of this noise on the inversion results.

Fig. 5 displays the salt model gradients for the FWI, DEI, and PDEI methods as applied to the model depicted in Fig. 3. The gradient from conventional FWI (Fig. 5(a)) effectively inverts only the upper boundary of the salt structure and struggles to recover the large-scale features of the salt dome. In contrast, the DEI method's gradient (Fig. 5(b)) demonstrates an ability to effectively recover the large-scale features throughout the salt structure, confirming its effectiveness in capturing the low-wavenumber components of the salt velocity model. However, a comparison of the DEI gradient with the true salt model indicates a deficiency in accurately depicting the salt-bottom boundary. This is mainly because envelope signals lack the phase information contained in seismic data. Phase information is crucial for inversion accuracy, as illustrated by the differing polarity of reflected wave: when seismic waves hit the top of the salt boundary, the reflected wave maintains its polarity, whereas at the salt-bottom, the polarity of the reflected wave inverts by 180°. Moreover, as waves transit through thin layers, interference and phase rotation alter the phase information. Consequently, integrating the traditional envelope signal with the phase information of seismic data becomes

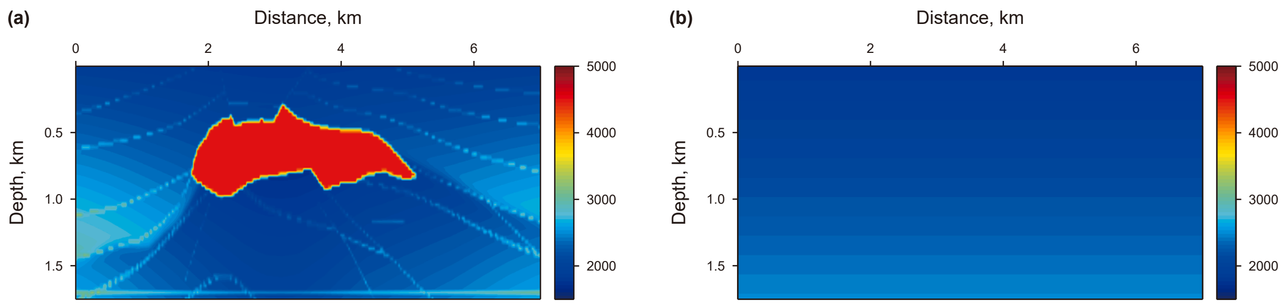

Fig. 3. Salt velocity models: **(a)** true velocity model, **(b)** initial velocity model.

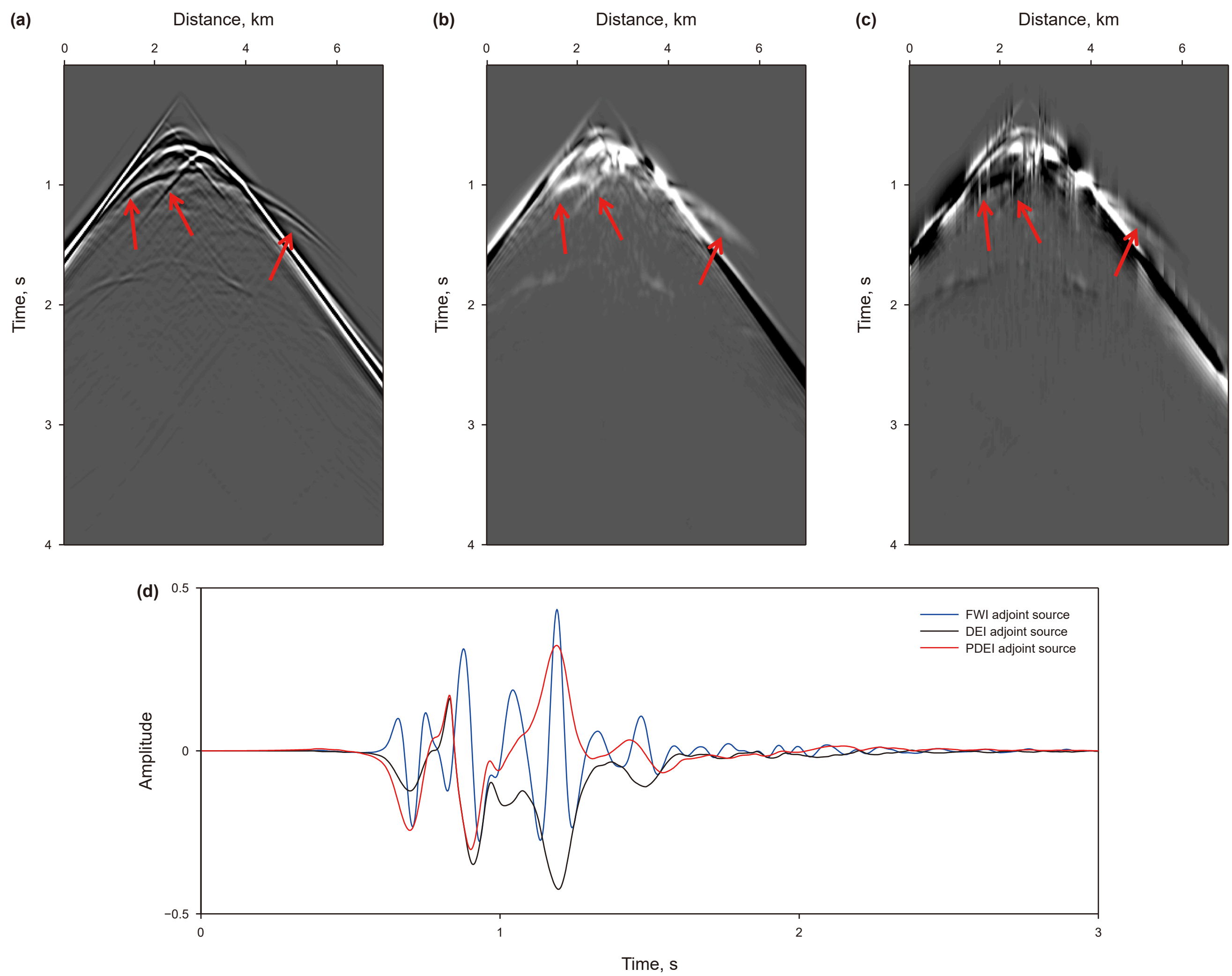

Fig. 4. Adjoint sources: **(a)** FWI adjoint source; **(b)** DEI adjoint source; **(c)** PDEI adjoint source; **(d)** comparative analysis of the three adjoint sources at the position of 2 km.

necessary for the precise inversion of strong-contrast models. The gradient produced by the PDEI method (Fig. 5(c)) successfully restores the low-wavenumber components of the salt structure and accurately delineates the salt-bottom boundary. This finding highlights the vital role of incorporating seismic data's phase information in the inversion process, affirming its essential contribution to obtaining precise model reconstructions. This emphasizes the need for approaches that merge phase information with traditional envelope inversion to improve accuracy in building complex geological structures.

3.2. Salt model inversion using common seismic data

To further compare the advantages of FWI, DEI, and TV-PDEI in recovering low-wavenumber velocity structures, we conducted tests using the salt model and acquisition system shown in Fig. 3.

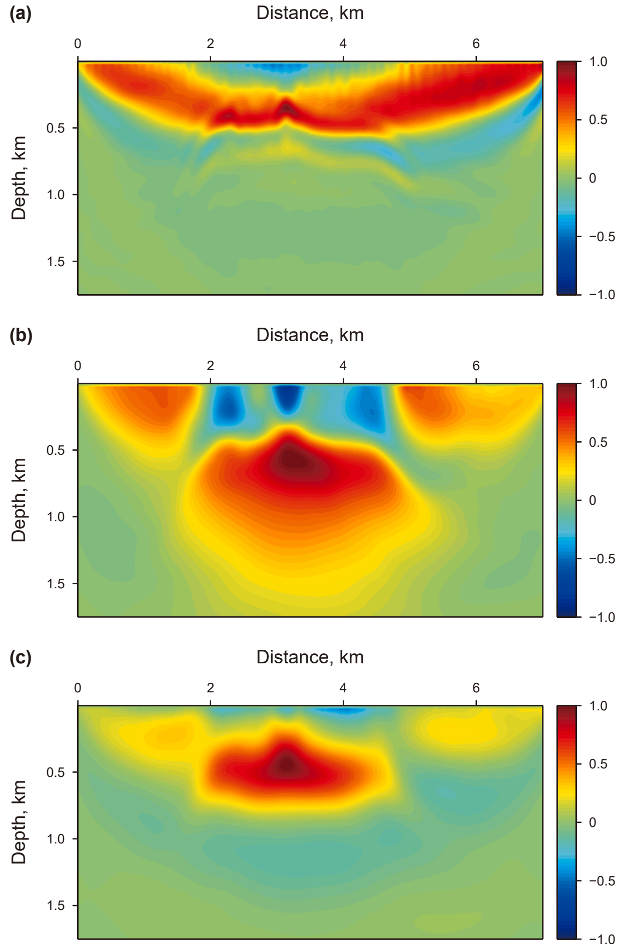

Fig. 5. Salt model gradients: **(a)** FWI gradient; **(b)** DEI gradient; **(c)** PDEI gradient.

To mitigate the cycle skipping issue often encountered in FWI, a multi-scale inversion strategy across frequency bands was employed. Fig. 6(a) shows the FWI result from low-frequency seismic data in the 4–6 Hz range. This result was then used as the initial velocity model for FWI with high-frequency data in the 4–15 Hz. The final velocity inversion result is depicted in Fig. 6(b). There are noticeable discrepancies between the final FWI result and the true salt model due to the absence of frequency below 4 Hz in the seismic data. Additionally, the Born approximation in FWI limits the accuracy of inversions for large-scale, strong-contrast velocity structures, leading to severe cycle skipping. This makes it challenging for FWI to achieve high-resolution results in such complex media.

The envelope signal contains abundant low-frequency components, which are closely linked to the low-wavenumber structures in the velocity model. Fig. 7(a) shows the DEI results, which successfully recover the large-scale structure of the salt dome owing to the low-frequency advantage of the envelope signal. However, due to the absence of phase information, the DEI method fails to accurately depict the salt-bottom. This is further illustrated by the gradient analysis in Fig. 5(b) for DEI. Next, using the inversion result from Fig. 7(a) as the initial velocity model, we conducted FWI on the 4–6 Hz low-frequency band, as shown in Fig. 7(b). Subsequently, the outcome from Fig. 7(b) served as the initial velocity model for FWI in the 4–15 Hz high-frequency band, resulting in the inversion shown in Fig. 7(c). The final DEI + multi-scale FWI inversion outcome reveals significant anomalies at the salt-bottom, primarily due to DEI's inability to accurately invert the salt-bottom information, leading to imprecise sub-salt velocity model building. Therefore, it is necessary to incorporate seismic phase information to compensate for the limitations of DEI, enhancing the accuracy of sub-salt velocity model building. This approach underscores the importance of integrating phase information with envelope inversion method to improve the accuracy of inversion in complex geological settings.

Fig. 8(a) illustrates the results of large-window PDEI (1500 ms and 900 ms), revealing that the inversion successfully inverts the large-scale salt bodies while accurately delineating the salt-bottom structure. In Fig. 8(b), using the results from Fig. 8(a) as the initial model, short-window PDEI (600 ms, 500 ms, 400 ms) result further refine the internal velocity of the salt structures, leading to velocity values that more closely approximate the true salt velocity. Subsequently, the inversion results from Fig. 8(b) are used as the initial velocity model for low-frequency (4–6 Hz) FWI, as shown in Fig. 8(c). The results from Fig. 8(c) serve as the initial velocity model for high-frequency (4–15 Hz) FWI inversion, as presented in Fig. 8(d). Compared to Figs. 7(c) and 8(d) demonstrates that the application of PDEI combined with multi-scale FWI has significantly improved the salt inversion results, thus validating the efficacy of PDEI method in building velocity model of salt domes and sub-salt structures. Nevertheless, it is observed that Fig. 8(a) and (b) exhibit noticeable inversion noise in the shallow sections, and the final sub-salt velocity inversion still displays discrepancies when compared to the true salt velocity model. To address these issues and enhance recovering accuracy for salt-bottom and subsalt velocities, it is necessary to incorporate total variation regularization methods.

To address the errors associated with waveform matching in PDEI, particularly the noise observed in the shallow inversion of Fig. 8(a) and (b), total variation regularization was incorporated into the PDEI misfit function. This approach mitigates the mismatch errors and enhances the stability of the inversion process. Fig. 9 demonstrates the effect of implementing a TV-PDEI regularization weighting factor $\lambda_{TV} = 1$. A comparison between

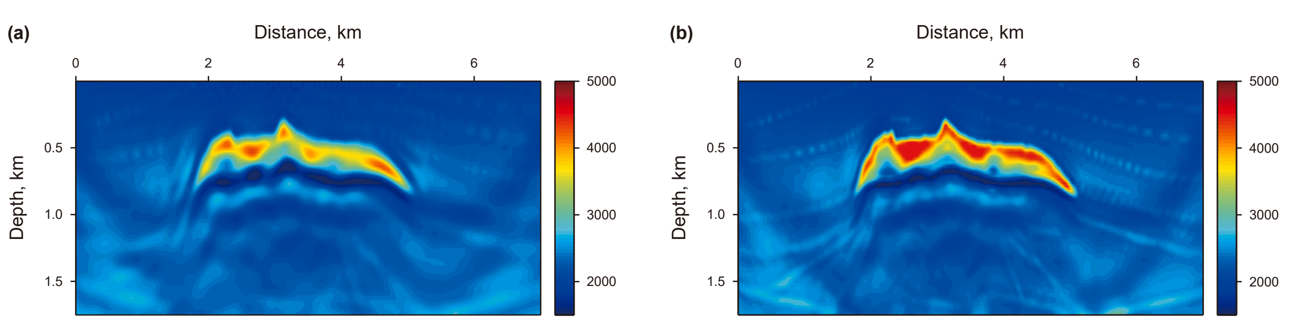

Fig. 6. FWI results: **(a)** low-frequency band FWI result (4–6 Hz); **(b)** multi-scale FWI result using Fig. 6(a) as the initial model.

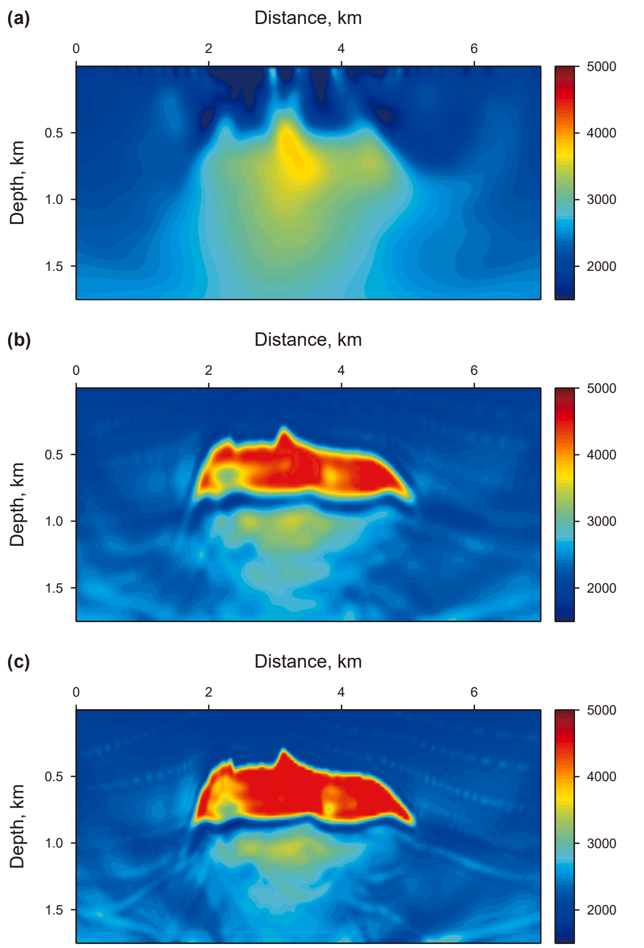

Fig. 7. DEI + FWI results: **(a)** DEI result; **(b)** low-frequency band FWI result (4–6 Hz) using Fig. 7(a) as the initial model; **(c)** multi-scale FWI result using Fig. 7(b) as the initial model.

Figs. 8(a) and 9(a), we highlight that the application of total variation regularization substantially reduces noise in the shallow regions of the velocity inversion. Additionally, the inverted velocity model exhibits increased smoothness and improved algorithm stability. As high-frequency seismic data are used, the resolution of the inversion result is improved (Fig. 9(c) and (d)). However, an overemphasis on regularization can result in the excessive smoothing of weak scattering interfaces within TV-PDEI results, potentially compromising model inversion accuracy (Fig. 9(d)).

Fig. 10 illustrates the results using the TV-PDEI regularization weighting factor $\lambda_{TV} = 0.6$. A comparison between Figs. 9 and 10 shows that with a weighting factor of $\lambda_{TV} = 0.6$, TV-PDEI not only achieves excellent inversion results for the salt dome boundaries, but also significantly improves the recovery of weak scattering interfaces when high-frequency seismic data are involved (Fig. 10(d)). By contrasting Fig. 8(d) with Figs. 9(d) and 10(d), it becomes apparent that regularization enhances the inversion accuracy for subsalt structures and notably refines the large-scale salt domes. The velocity profile comparison in Fig. 11 reveals that the TV-DEI combined with multi-scale TV-FWI and regularization weighting factors delivers the results closest to the true velocities in sub-salt velocity inversion. These comparative analyses across DEI, PDEI, and TV-PDEI confirm the notable benefits of the proposed TV-PDEI method in effectively inverting the velocities of large-scale, strong-contrast salt-bottom and subsalt structures.

However, reconstructing polarity envelope signals can occasionally alter the original signal characteristics, inevitably introducing disturbances. In conventional single-shot seismic data acquisition, such disturbances can be effectively minimized through multi-shot stacking, obtaining high-resolution inversion results for strongly scattering salt structures. Conversely, simultaneous source acquisition poses cross-talk noise challenges that can significantly disrupt the low-wavenumber velocity inversion of salt structures during polarity envelope reconstruction. To enhance computational efficiency and increase the stability of the simultaneous source PDEI algorithm, a comparative analysis

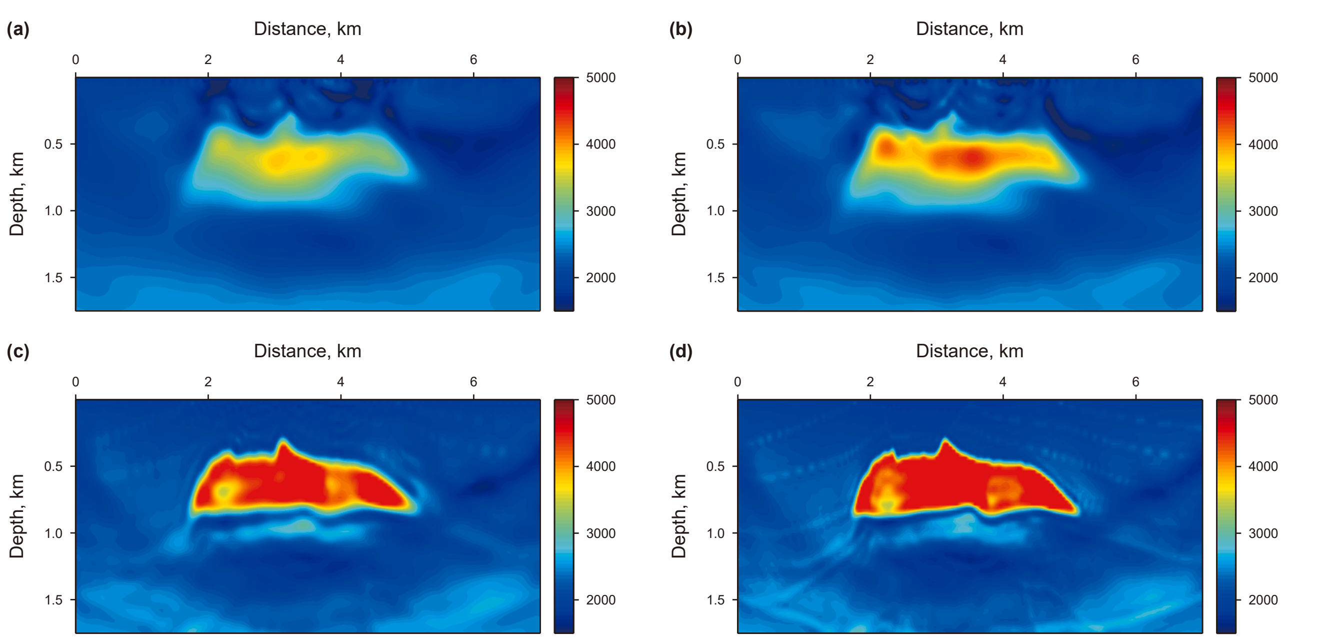

Fig. 8. PDEI + FWI results: **(a)** large-window PDEI result (1500 ms and 900 ms); **(b)** short-window PDEI (600 ms, 500 ms, 400 ms) using Fig. 8(a) as the initial model; **(c)** low-frequency band FWI result (4–6 Hz) using Fig. 8(b) as the initial model; **(d)** multi-scale FWI result using Fig. 8(c) as the initial model.

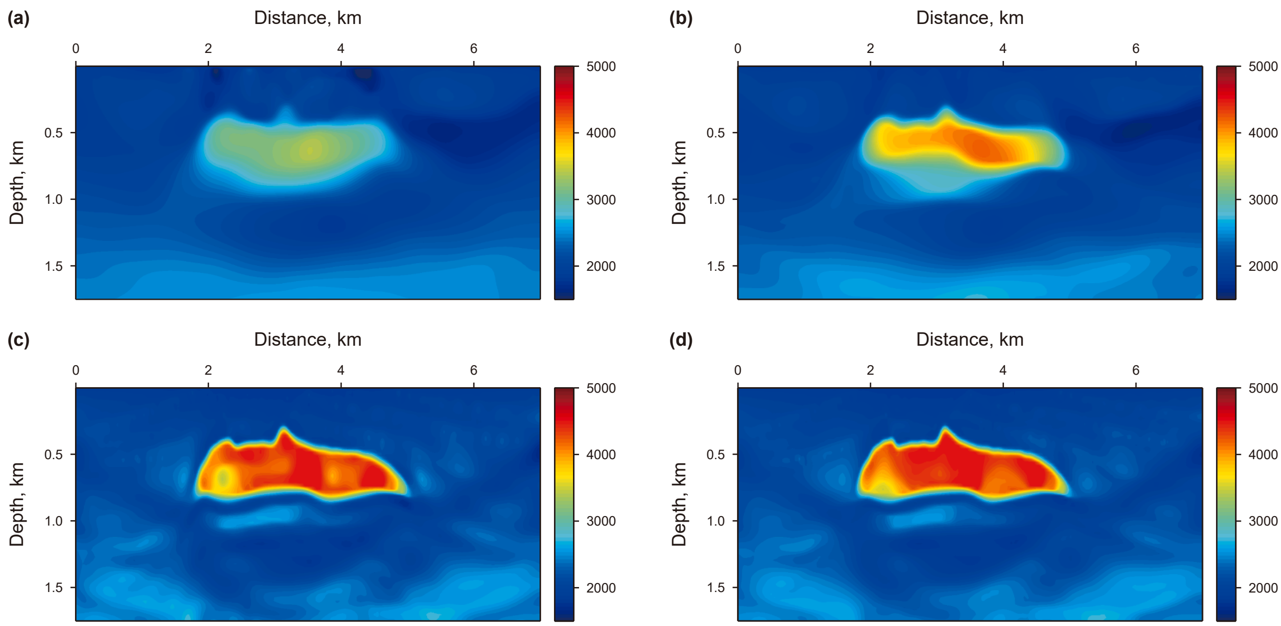

Fig. 9. TV-PDEI + FWI results ($\lambda_{TV} = 1$): **(a)** large-window TV-PDEI result (1500 ms and 900 ms); **(b)** short-window TV-PDEI result (600 ms, 500 ms, 400 ms) using Fig. 9(a) as the initial model; **(c)** low-frequency band FWI result (4–6 Hz) using Fig. 9(b) as the initial model; **(d)** Multi-scale FWI result using Fig. 9(c) as the initial model.

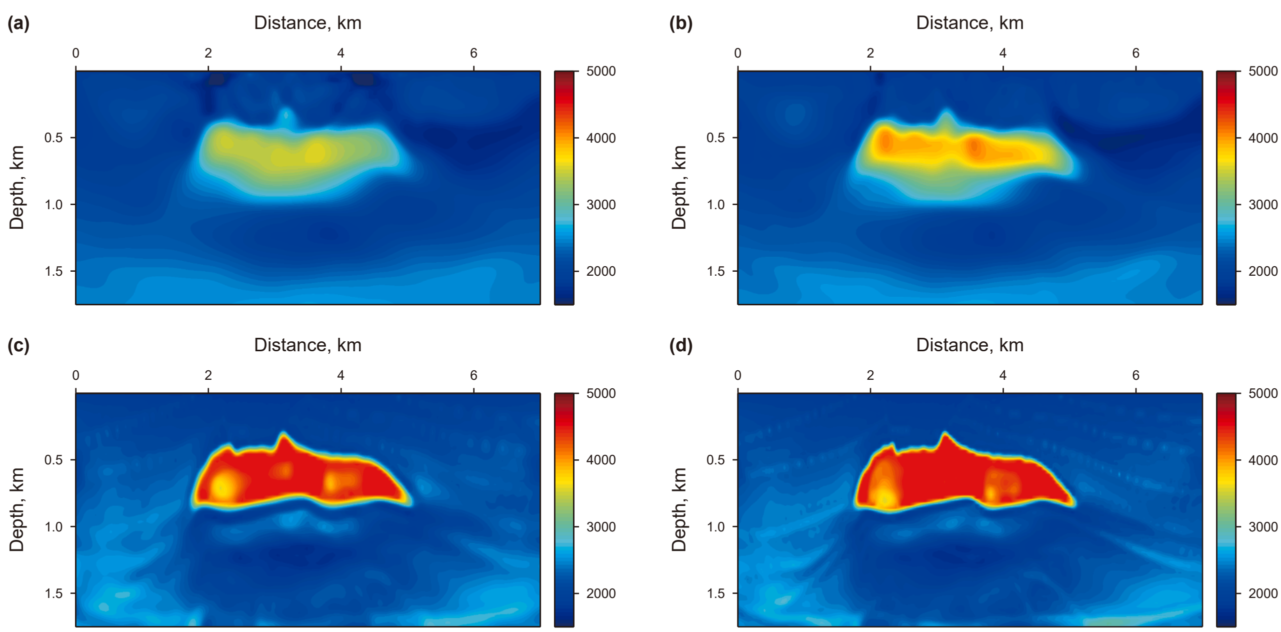

Fig. 10. TV-PDEI + FWI results ($\lambda_{TV} = 0.6$): **(a)** large-window TV-PDEI result (1500 ms and 900 ms); **(b)** short-window TV-PDEI result (600 ms, 500 ms, 400 ms) using Fig. 10(a) as the initial model; **(c)** low-frequency band FWI result (4–6 Hz) using Fig. 10(b) as the initial model; **(d)** multi-scale FWI result using Fig. 10(c) as the initial model.

of the simultaneous source TV-PDEI method will be conducted next.

3.3. Salt model inversion using simultaneous source seismic data

In order to test the challenges of the PDEI method with simultaneous source seismic data and the advantages of the TV-PDEI method in low wavenumber velocity model building, this section utilizes the salt velocity model shown in Fig. 3 for testing. In this section, we evaluate the inversion performance of several methods: simultaneous source FWI, simultaneous source DEI, and simultaneous source TV-PDEI. Given the setup of 280 sources and their corresponding receivers on the surface, use of all sources during inversion would demand enormous computational resources. To enhance efficiency, we group multiple sources into “super-shots”, forming a total of 10 super-shots. Moreover, dynamic position encoding alongside dynamic amplitude-phase encoding is employed to alleviate cross-talk noise inherent in simultaneous source acquisition. Dynamic encoding involves periodically changing the position, amplitude, and phase information of sources every six iterations during the process of updating the velocity model. This strategy ensures the effective utilization of the complete set of 280 sources while substantially reducing computational demands. Fig. 12 illustrates the source combinations corresponding to the 1st, 5th, and 10th super-shots. Each super-shot displays randomly distributed source positions,

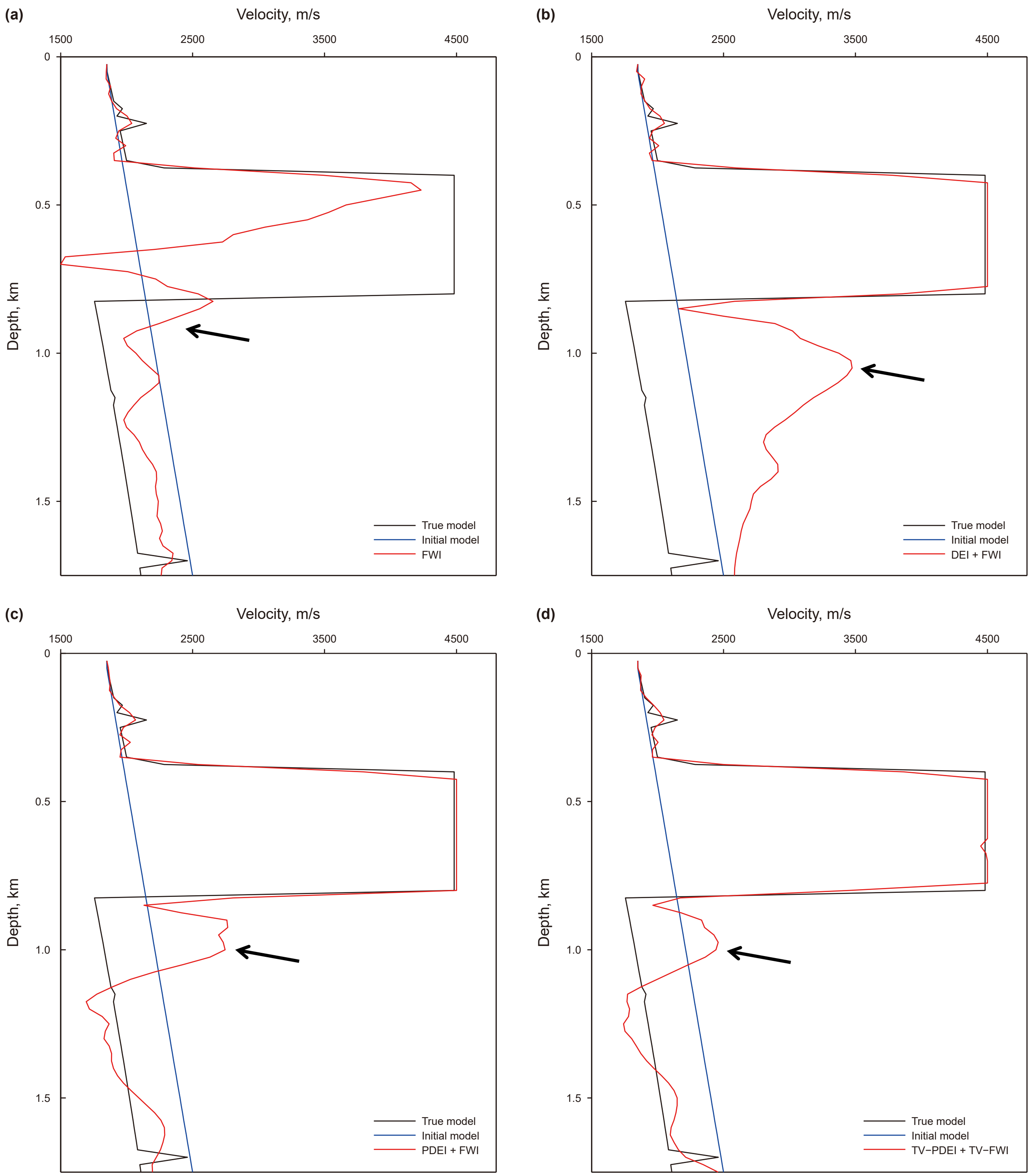

Fig. 11. Velocity profiles of inversion results at distance of 2 km: **(a)** multi-scale FWI result; **(b)** DEI + Multi-scale FWI result; **(c)** PDEI + multi-scale FWI result; **(d)** TV-PDEI + multi-scale TV-FWI result with $\lambda_{TV} = 0.6$.

amplitudes, and phases, with phases appearing randomly as positive and negative. This approach significantly enhances FWI computational efficiency while minimizing cross-talk noise for simultaneous source seismic data inversion.

Fig. 13 presents the results of multi-scale simultaneous source FWI. The initial velocity model is obtained using low-frequency seismic data in the 4–6 Hz, and subsequently, high-resolution inversion results are achieved by incorporating high-frequency seismic data in the 4–15 Hz. Upon comparing Fig. 6(b) with Fig. 13(b), it is evident that the strategy of dynamic random encoding effectively mitigates the impact of crosstalk noise. This approach allows simultaneous source FWI to yield high-resolution inversion results. However, due to the absence of low-frequency components below 4 Hz in the seismic data, simultaneous source FWI encounters significant cycle-skipping issues during waveform matching. This challenge makes it difficult for the FWI method to achieve high-resolution inversion results for large-scale, strong-contrast media. Therefore, leveraging the advantages of low-frequency envelope information is crucial for obtaining accurate inversion results for strong-contrast salt velocity models.

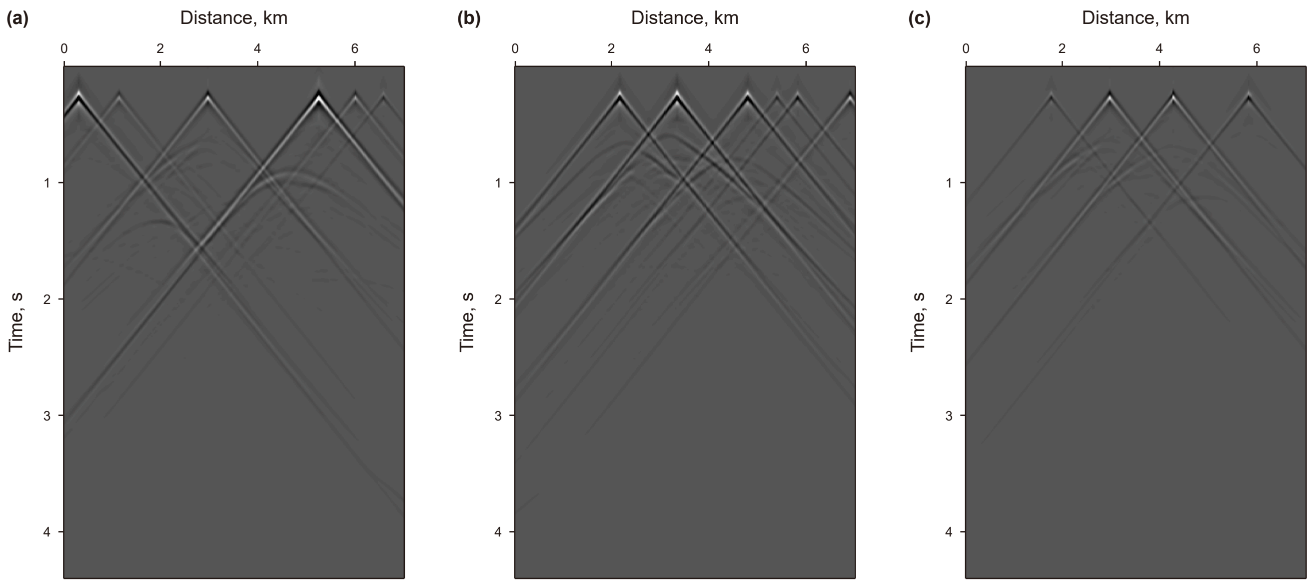

Fig. 12. Simultaneous source seismic data. **(a)** The 1st super-shot; **(b)** the 5th super-shot; **(c)** the 10th super-shot.

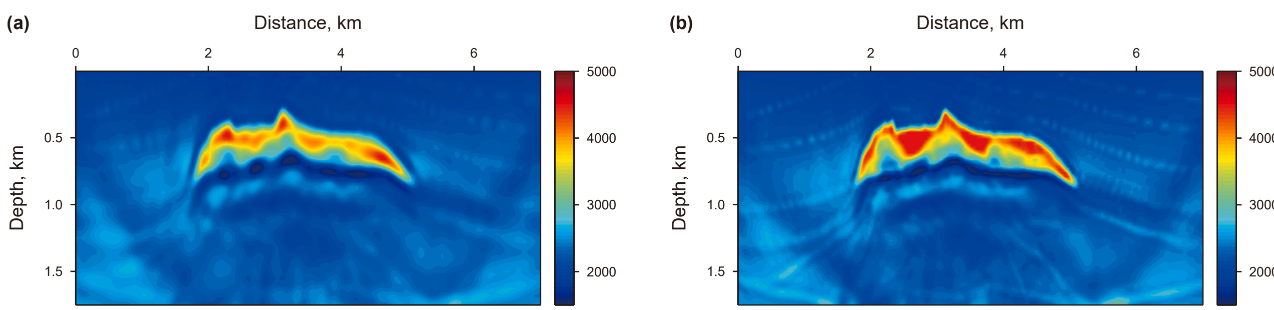

Fig. 13. Simultaneous source FWI results. **(a)** Low-frequency band FWI result (4–6 Hz); **(b)** multi-scale FWI result using Fig. 13(a) as the initial model.

Fig. 14 illustrates the results from simultaneous source DEI. Due to the absence of phase information in the envelope data, the salt-bottom is not well inverted, as shown in Fig. 14(a). Using the inversion result from Fig. 14(a) as the initial velocity model for FWI in the 4–6 Hz low-frequency band, the inversion result is as depicted in Fig. 14(b). This result then serves as the initial model for FWI in the 4–15 Hz high-frequency band, as shown in Fig. 14(c). It is apparent from the final inversion results of simultaneous source DEI + multi-scale simultaneous source FWI that significant velocity anomalies persist at the subsalt. This is primarily because the DEI method fails to accurately invert the salt-bottom boundary. The results from simultaneous source large-window TV-PDEI are shown in Fig. 15, which illustrates that as the regularization weight factor decreases, the PDEI is severely affected by crosstalk noise generated by the simultaneous source seismic data (Fig. 15(d)). While the simultaneous source PDEI employed a dynamic encoding strategy, errors introduced during the polarity envelope reconstruction process further amplify the impact of the simultaneous source crosstalk noise (Fig. 15(d)), hindering accurate inversion of the strongly scattering salt structures. Thus, enhancing PDEI computational efficiency with simultaneous source seismic data necessitates incorporating regularization algorithms to suppress cross-talk noises.

To further improve the inversion resolution of the salt structures, Fig. 15 is then used as the initial velocity models for short-window TV-PDEI (600 ms, 500 ms and 400 ms), shown in Fig. 16. As the reconstruction window length for the polarity envelope is reduced, the resolution of the corresponding TV-PDEI results improves significantly. A comparison between Figs. 16(b) and 10(b) indicates that the simultaneous source TV-PDEI results are similar to those of the common single-shot based PDEI result, largely unaffected by simultaneous source crosstalk noise. A comparison between Figs. 8(b) and 16(d) shows that without regularization, simultaneous source PDEI suffers from severe crosstalk noise, failing to invert the low wavenumber components of the salt structures. Using Fig. 16(b) as the initial velocity model for FWI in the 4–6 Hz low-frequency band yields the results in Fig. 17(a), which is then refined using the 4–15 Hz high-frequency band FWI, resulting in Fig. 17(b). A comparison between Figs. 8(d), 10(d) and 17(b) shows that the final inversion results of simultaneous source TV-DEI + multi-scale simultaneous source FWI resemble those of the common single-shot based PDEI result. Therefore, while utilizing simultaneous source to improve PDEI computational efficiency, it is essential to use regularization methods to alleviate the impact of crosstalk noise on PDEI results.

3.4. Simultaneous sources-based salt model inversion using noisy seismic data

In this section, we introduce Gaussian noise into the observed data to evaluate the noise robustness of the simultaneous source-based PDEI and TV-PDEI methods. Fig. 18 presents three sets of

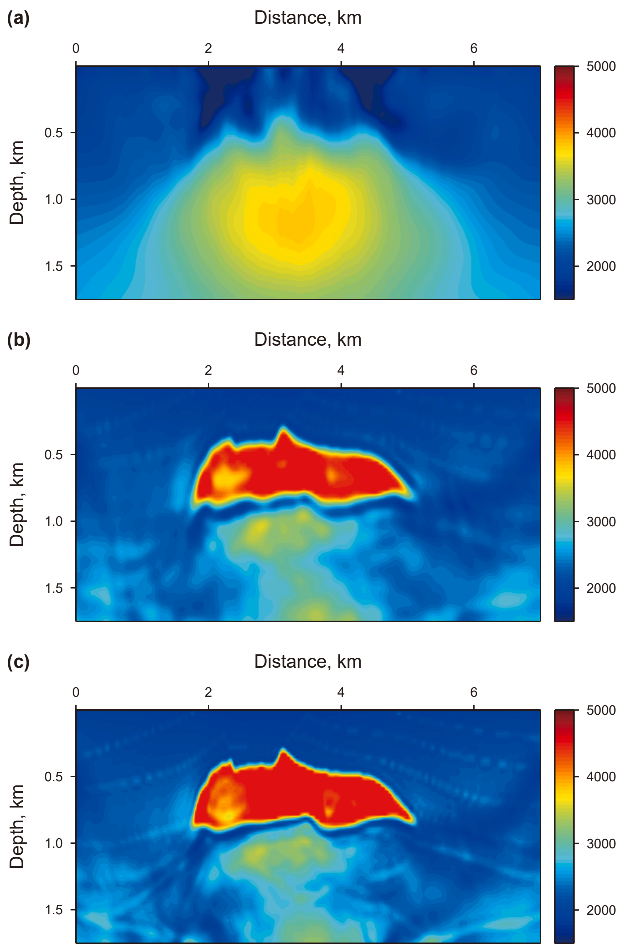

Fig. 14. Simultaneous source DEI + simultaneous source FWI results. **(a)** DEI result; **(b)** low-frequency band FWI result (4–6 Hz) using Fig. 14(a) as the initial model; **(c)** multi-scale FWI result using Fig. 14(b) as the initial model.

noisy seismic data obtained from simultaneous source, clearly showing the presence of significant noise interference. Despite the strong Gaussian noise environment, Figs. 19 and 20 depict the inversion results of the simultaneous source-based PDEI and TV-PDEI methods, which still successfully reconstruct the salt dome structure with considerable resolution. Initially, we tested the simultaneous source-based TV-PDEI method using larger window lengths of 1500 ms and 900 ms, as shown in Fig. 19. It is evident that as the regularization weight factors decrease, the TV-PDEI results become increasingly susceptible to random noise and simultaneous source noise interference. To further enhance the resolution of the salt structure inversion, we employed the inversion results from Fig. 19 as initial velocity models for short-window TV-PDEI (600 ms, 500 ms, 400 ms), with results illustrated in Fig. 20. The resolution of the resulting TV-PDEI significantly improves as the window length decreases. A comparison between Figs. 15(a)–(c) and 19(a)–(c) indicates that the TV-PDEI results are predominantly unaffected by random noise and simultaneous source crosstalk noise. Moreover, when comparing Figs. 8(b) and 20(d), it is apparent that the PDEI results without total variation constraints suffer considerably from simultaneous source and random noise interference, particularly in the velocity inversion at the salt bottom. The comparative analysis of Figs. 19 and 20 underscores the TV-PDEI method's capacity to effectively resist Gaussian noise during the inversion process, thereby producing more accurate inversion results.

4. Application to SEG 2014 Chevron blind test dataset

We applied the FWI, DEI and PDEI methods to the SEG 2014 Chevron blind test dataset for evaluation. The dataset consists of seismic data generated through forward modeling using the elastic wave equation, with marine streamer acquisition. The low-frequency band of this data contains significant random noise and free-surface multiples. The complete dataset comprises 1600 shots, with source depths at 15 m. The first shot is located at 1 km, with a shot interval of 25 m, and the last shot at 40.975 km. Each

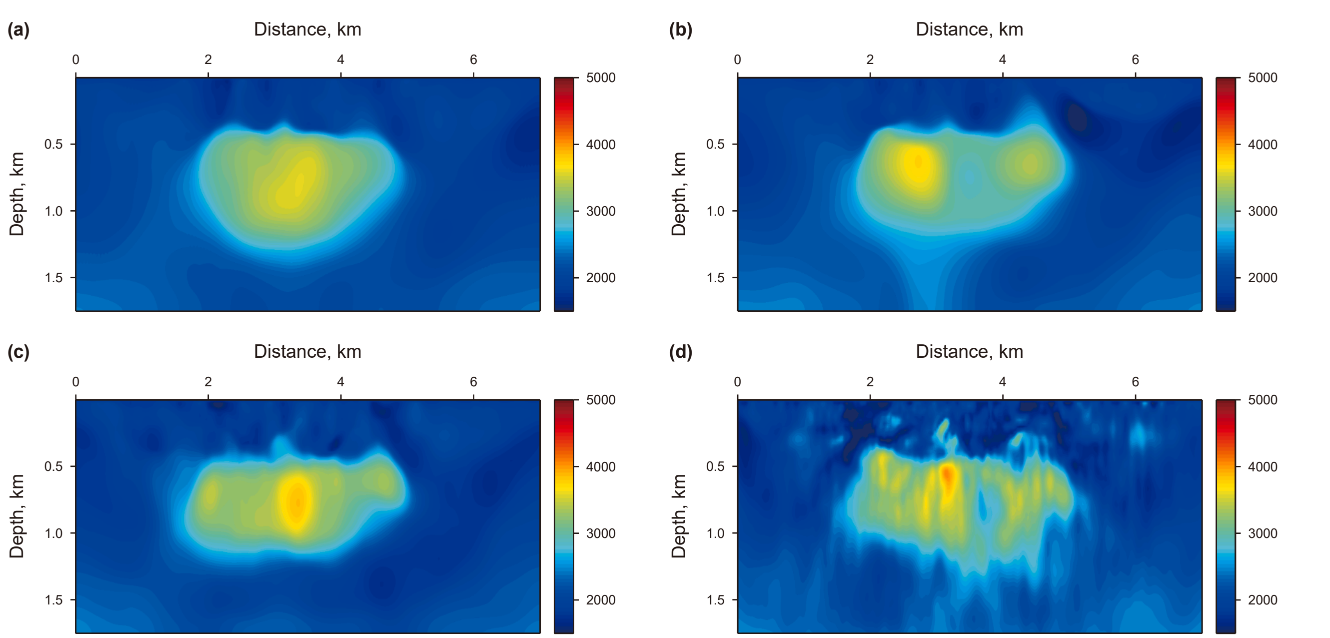

Fig. 15. Simultaneous source large-window TV-PDEI (with window length of 1500 ms and 900 ms) results with different weighting factors: **(a)** $\lambda_{\mathrm{TV}} = 1$; **(b)** $\lambda_{\mathrm{TV}} = 0.6$; **(c)** $\lambda_{\mathrm{TV}} = 0.3$; **(d)** $\lambda_{\mathrm{TV}} = 0$.

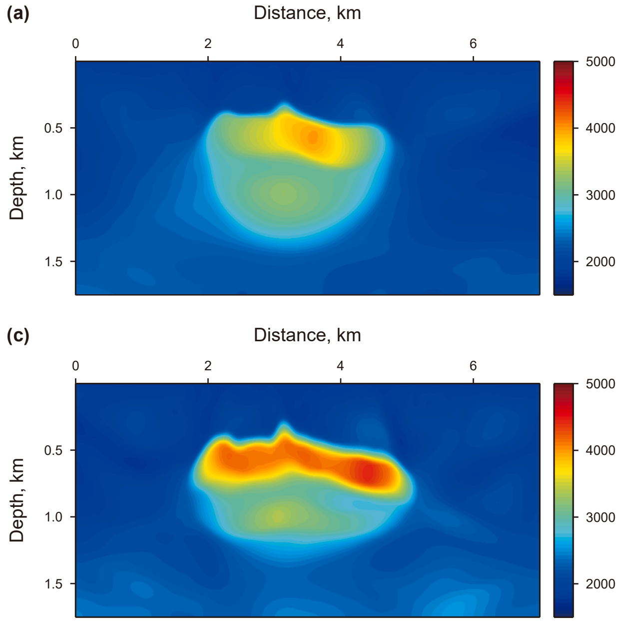

Fig. 16. Simultaneous source short-window TV-PDEI (600 ms, 500 ms and 400 ms) results with different weighting factors using Fig. 15 as the initial models, **(a)** $\lambda_{TV} = 1$; **(b)** $\lambda_{TV} = 0.6$; **(c)** $\lambda_{TV} = 0.3$; **(d)** $\lambda_{TV} = 0$.

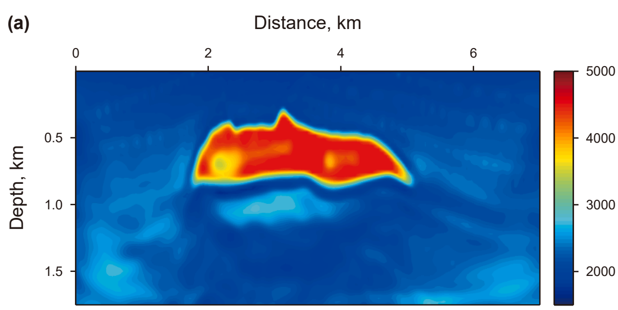

Fig. 17. Multi-scale simultaneous source TV-FWI with weighting factor $\lambda_{TV} = 0.3$. **(a)** Low-frequency band FWI result (4–6 Hz) using Fig. 16(b) as the initial model; **(b)** multi-scale FWI result using Fig. 17(a) as the initial model.

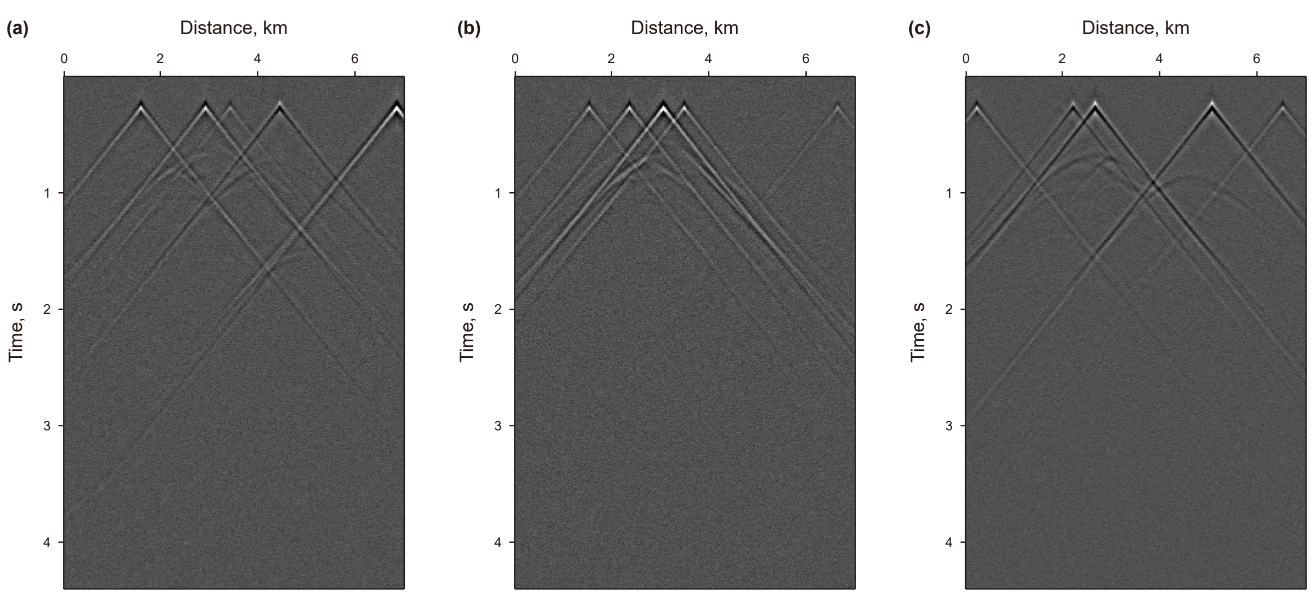

Fig. 18. The simultaneous source seismic data with Gaussian noise: **(a)** the 1st super-shot; **(b)** the 5th super-shot; **(c)** the 10th super-shot.

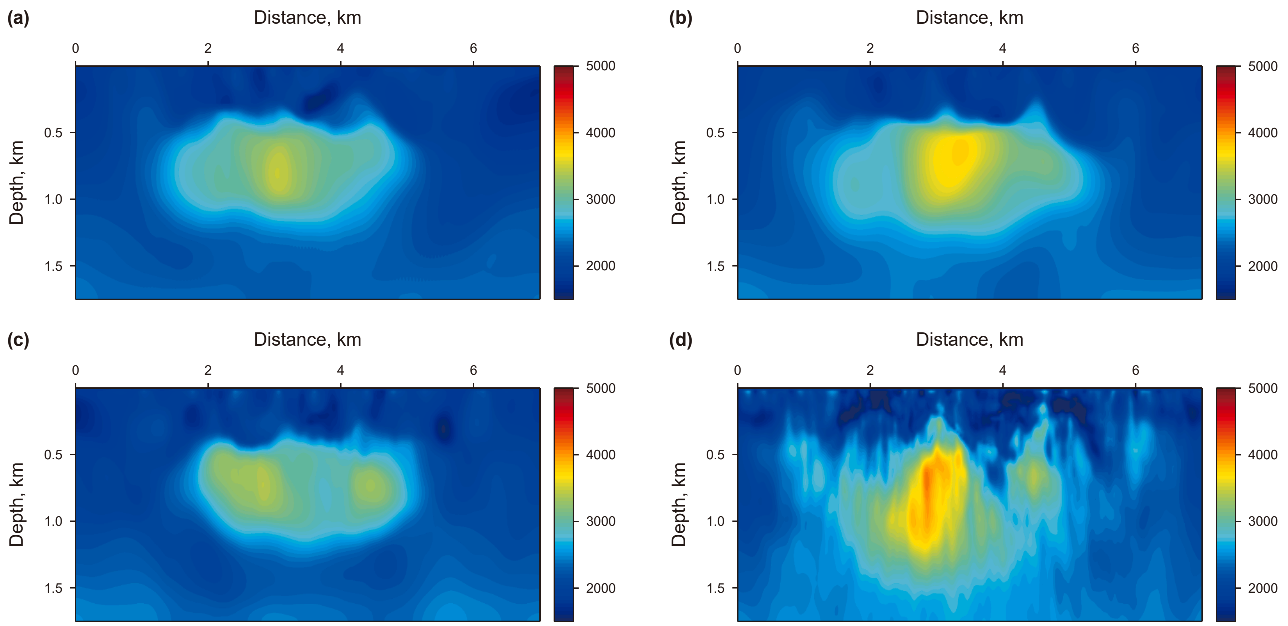

Fig. 19. Simultaneous source large-window TV-PDEI results (1500 ms and 900 ms) with noisy seismic data and different weighting factors: **(a)** $\lambda_{TV} = 1$; **(b)** $\lambda_{TV} = 0.6$; **(c)** $\lambda_{TV} = 0.3$; **(d)** $\lambda_{TV} = 0$.

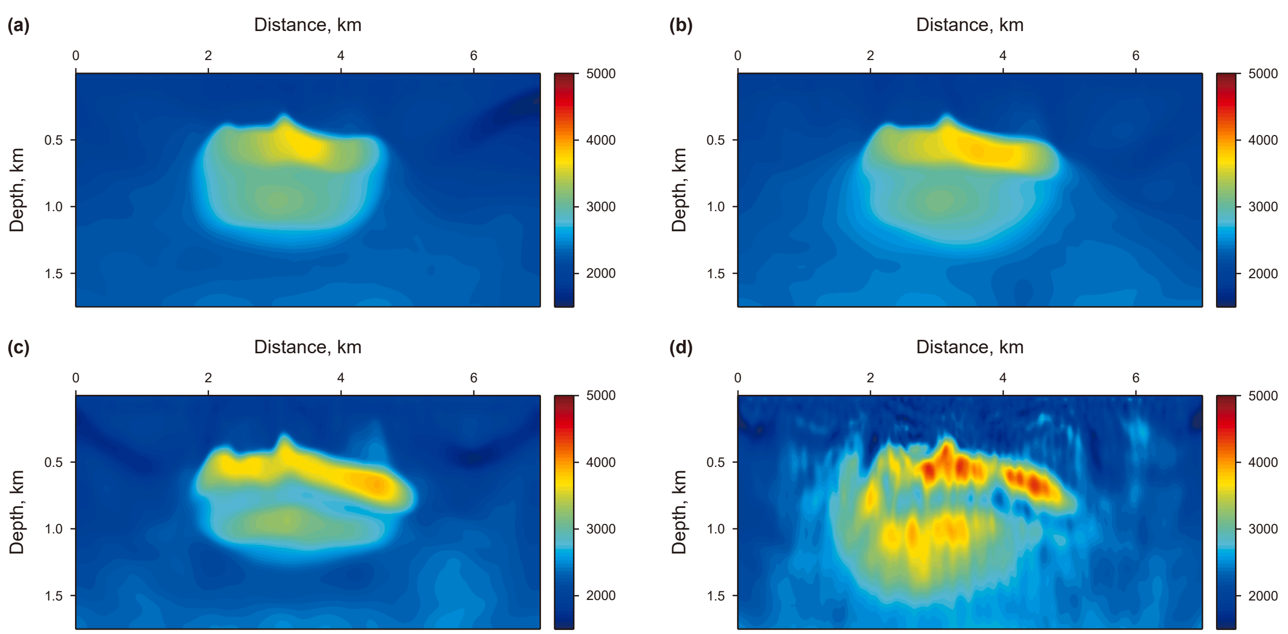

Fig. 20. Simultaneous source short-window TV-PDEI results (600 ms, 500 ms and 400 ms) with noisy seismic data and different weighting factors: **(a)** $\lambda_{TV} = 1$; **(b)** $\lambda_{TV} = 0.6$; **(c)** $\lambda_{TV} = 0.3$; **(d)** $\lambda_{TV} = 0$.

shot includes 321 receivers, spaced at 25 m, also at a depth of 15 m. The initial velocity model is shown in Fig. 21(a). We conducted FWI tests starting with seismic data in the 0–4 Hz frequency band, incrementally increasing by 1 Hz, and continuing until the seismic data in the 0–10 Hz frequency band was fully inverted.

Given the substantial computational demand presented by the 1600 shots, we enhanced computational efficiency by combining 8 shots into one simultaneous source, as illustrated in Fig. 21(b). In a streamer acquisition system, all receivers move forward by one position each time the shot point is relocated. This characteristic allows us to consolidate seismic data from 8 adjacent shots into one dataset, creating a simultaneous source seismic dataset. However, it necessitates discarding some seismic data at both ends of the 8 km streamer, yielding a useable simultaneous source dataset spanning 7.825 km. This minor reduction in seismic data did not notably affect the inversion results but enhanced computational efficiency eightfold, which is highly advantageous.

Fig. 22 shows the low-frequency band (0–4 Hz) data from the SEG 2014 Chevron blind test dataset. It reveals that the original data in the 0–4 Hz frequency band contains substantial low-frequency noise, presenting a considerable challenge for FWI methods, which heavily depend on low frequencies. By consolidating the 8 sources into one simultaneous source seismic data set, we achieved a notable increase in the signal-to-noise ratio of

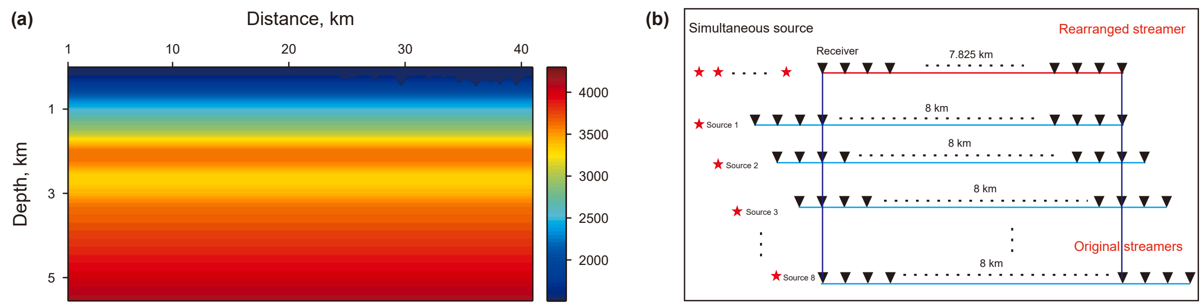

Fig. 21. **(a)** Initial velocity model; **(b)** simultaneous source marine streamer acquisition system formed by combining 8 sources.

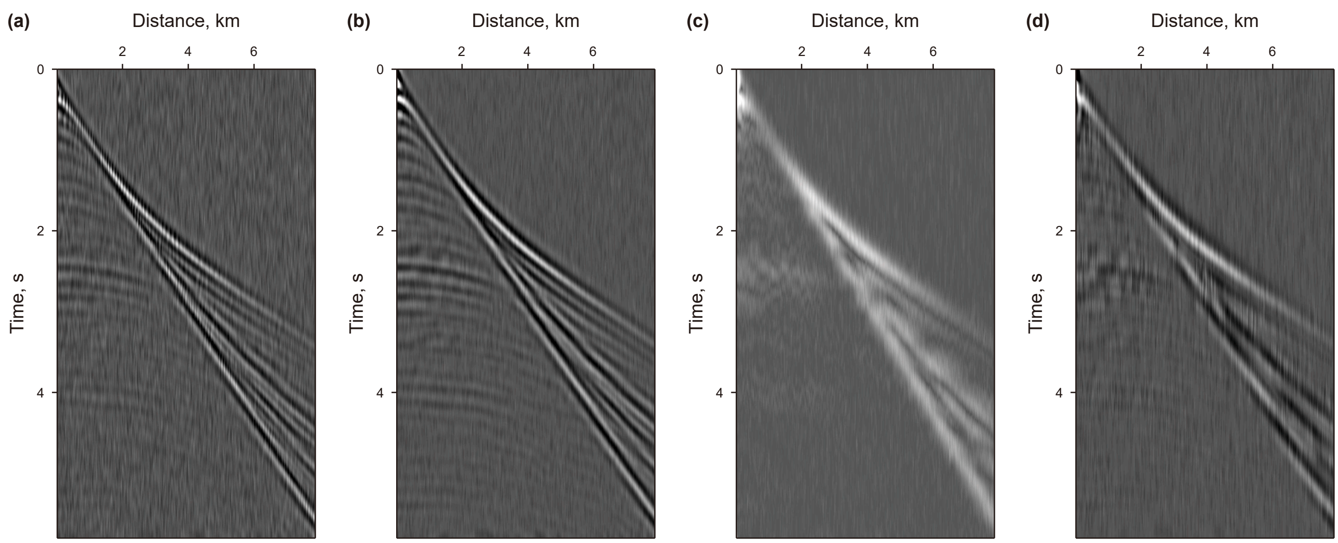

Fig. 22. Low-frequency band (0–4 Hz) of SEG 2014 Chevron blind test dataset: **(a)** original shot records from the 161th source; **(b)** simultaneous source seismic data formed by combining 8 sources (from the 161th to 168th sources); **(c)** envelope of the simultaneous source seismic data; **(d)** polarity envelope of the simultaneous source seismic data.

reflected waves and some attenuation of random noise, while also enhancing deep reflection energy. More importantly, the simultaneous source formed through source combination significantly improved computational efficiency. The envelope of the simultaneous source observed data (Fig. 22(c)) shows broader waveform shapes, indicating rich low-frequency components but a loss of instantaneous phase information from the original data. The polarity envelope of the simultaneous source observed data (Fig. 22(d)) shows broad waveforms while preserving polarity information consistent with the original waveform data, suggesting the polarity envelope contains not only abundant low-frequency components but also instantaneous phase information from the original data.

We began the inversion process using low-frequency signals in the 0–4 Hz band, utilizing the initial model shown in Fig. 21(a). The first-step gradients are displayed in Fig. 23. By referencing previous inversion results (Almomin and Biondi, 2015; Warner and Guasch, 2015; Métivier et al., 2016; Vigh et al., 2016; Sun and Alkhalifah, 2019; Yong et al., 2019; Yong et al., 2023), we can analyze the accuracy of these gradients. Within the red box on the left side of the model, the velocity pertains to a large-scale high-velocity body, and the associated gradient should be positive. The DEI and PDEI methods with a 1.2 s window achieved correct velocity updates, demonstrating their efficacy in extracting accurate low-wavenumber components for large-scale structures. However, the FWI gradient displayed negative errors (Fig. 23(a)), and neither PDEI with 0.4 s nor 0.8 s windows succeeded in obtaining correct velocity updates (Fig. 23(c) and (d)). Notably, the gradient from PDEI with a 0.4 s window closely resembles the FWI gradient, which effectively validates the notion that shortening the window length results in polarity envelopes becoming closer to waveform data, causing the gradients to converge towards those of FWI result. In the central black box of the model, containing small-scale low-velocity and high-velocity bodies, both FWI and PDEI methods successfully obtained correct velocity updates. However, the DEI method, relying on envelope signals that lack instantaneous phase information, erroneously inverted the low-velocity body into a high-velocity one (Fig. 23(b)). On the right side of the model, within the red dashed box, the velocities pertain to large-scale low-velocity structures, where the gradient is expected to be negative. PDEI with 1.2 s and 0.8 s windows succeeded in achieving accurate velocity updates, underscoring their capability in obtaining correct low-wavenumber components for such large-scale structures. Yet, the FWI and PDEI with a 0.4s window gradient (Fig. 23(a) and (c)) displayed erroneous positive values in certain local regions, primarily driven by seismic data lacking high signal-to-noise ratio low-frequency components. More critically, DEI exhibited completely incorrect velocity updates in this area, which is the motivation for developing the PDEI method in this study.

The gradient comparison results reveal that the DEI method is particularly suited for reconstructing large-scale, strongly scattering high-velocity anomalies, such as salt dome structures. However, when large-scale low-velocity anomalies are present,

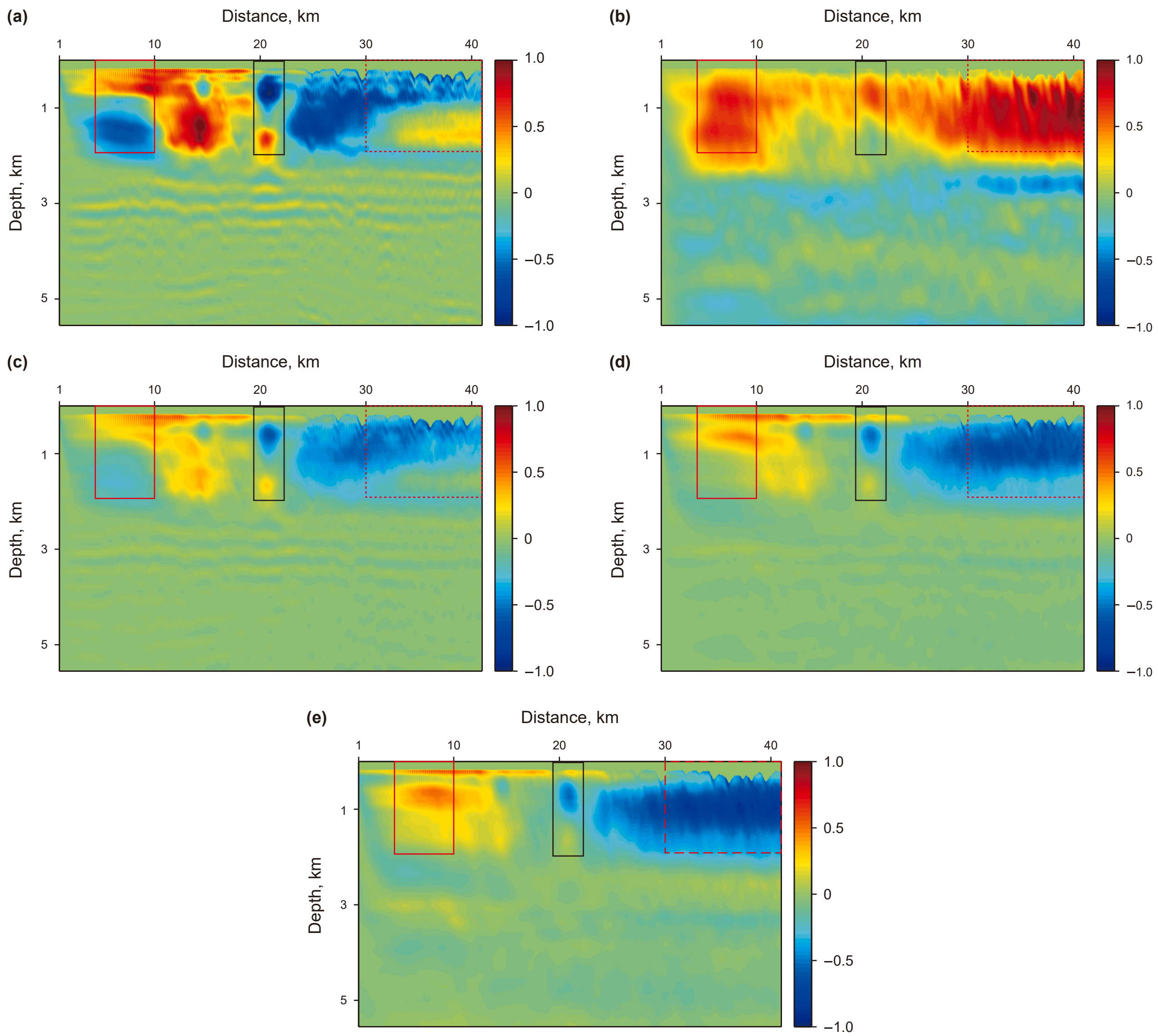

Fig. 23. The first-step gradients of different methods: **(a)** FWI; **(b)** DEI; **(c)** PDEI with a 0.4s window; **(d)** PDEI with a 0.8 s window; **(e)** PDEI with a 1.2 s window.

DEI's lack of phase information leads to incorrect velocity updates. In situations where seismic data lack low-frequency content, both FWI and short window (0.4 s and 0.8 s) PDEI methods are effective in accurately updating velocities for small-scale structures. Nevertheless, they struggle with large-scale structures, failing to invert their low-wavenumber components accurately. Conversely, larger window (1.2 s) PDEI method can successfully obtain low-wavenumber components for large-scale structures. As the number of iterations increases, gradually reducing the window length for PDEI enables high-resolution inversion results for subsurface velocity structures.

Fig. 24 presents the velocity inversion results for the low-frequency band (0–4 Hz). In Fig. 24(a), the FWI method successfully inverted small-scale structures, such as the three shallow low-velocity bodies and the undulating upper boundary of the high-velocity layer at a depth of 2 km. However, significant errors are evident at the model's left side near 10 km and the right side near 40 km, as well as in the inability to accurately invert the low-velocity layer at the depth of 2.5 km. These inaccuracies are primarily due to the absence of effective low-frequency components in the seismic data, hindering the accurate retrieval of low-wavenumber components for large-scale structures. Fig. 24(b) displays the DEI results, where correct velocity updates occur in the model's left region. However, in the right low-velocity zone and the three shallow low-velocity bodies, velocities update incorrectly. This is mainly due to the DEI method's insufficient utilization of the seismic data's phase information, leading to erroneous velocity update. Interestingly, at a depth of 2.5 km in the low-velocity region, the DEI method appears to achieve the correct update direction, potentially because the phase of diffracted or reflected waves at the base of the low-velocity region remains unchanged, facilitating accurate velocity updates.

To mitigate cycle-skipping issues associated with FWI, the TV-PDEI method with a 1.2 s Gaussian window was initially employed to invert the velocity model's low-wavenumber components. Subsequently, the Gaussian window length was progressively reduced, implementing a Multi-scale TV-PDEI approach (Fig. 24(c)). As shown, accurate inversion results are achieved for the high-velocity structures at 10 km on the left, the low-velocity zone between 30 and 40 km on the right, and the three shallow low-velocity bodies. These findings illustrate the significant advantages of the multi-scale TV-PDEI method in obtaining good

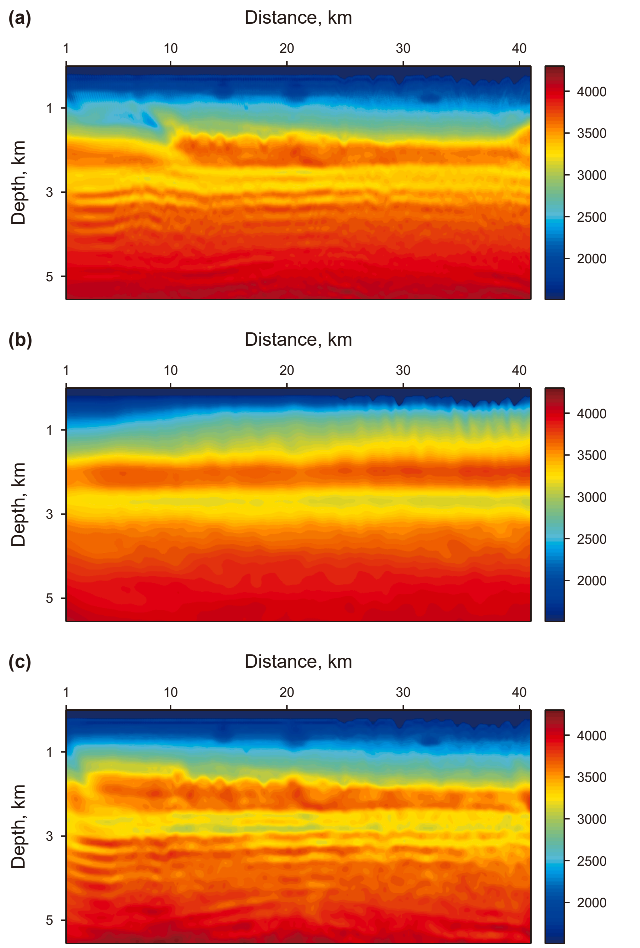

Fig. 24. Low-frequency band (0–4 Hz) inversion results. **(a)** FWI result; **(b)** DEI result; **(c)** Multi-scale TV-PDEI result with weighting factor $\lambda_{TV} = 0.6$ (with window length of 1.2 s, 0.8 s, 0.4 s).

initial velocity models, providing a robust foundation for Multi-scale FWI and effectively mitigating the cycle-skipping issue.

Utilizing the inversion results from the low-frequency band (Fig. 24(a) and (c)) as initial velocity models, a high-frequency band Multi-scale FWI was subsequently conducted, with the results displayed in Fig. 25. Fig. 25(a) illustrates that the incorporation of high-frequency information significantly enhances the resolution of the inversion results. However, in areas where velocity updates were incorrect during the low-frequency inversion, the high-frequency inversion results failed to show improvement. Additionally, the low-velocity layer at a depth of 2.5 km remains inaccurately inverted. In contrast, Fig. 25(b) shows a notable improvement compared to the Multi-scale FWI. Especially at the depth of 2.5 km, the low-velocity layer was accurately inverted using Multi-scale TV-PDEI combined with multi-scale TV-FWI. This validates the efficacy of TV-PDEI method, demonstrating its ability to achieve high-resolution inversion results even when low-frequency information is lacking and the initial velocity model is far from true model.

Fig. 26 compares the inversion results with well-log velocities, revealing that well-log velocities exhibit high precision and significant oscillations, reflecting the fine structural details of the subsurface. Achieving similarly detailed velocity structures with FWI requires a finely discretized mesh to satisfy the stability conditions of finite-difference wave equation modeling, significantly increasing computational resources. In this study, considering the balance between calculation resolution and computational resources, only seismic data in the 0–10 Hz frequency band were inverted. In Fig. 26, the initial velocity model provided relatively high-velocity values, presenting a substantial challenge to velocity inversion. The FWI results effectively inverted shallow region velocities, aligning well with the trend of the true velocity curves. However, the FWI velocity curves poorly fit the true velocity values in deep space. In contrast, the results from multi-scale PDEI combined with multi-scale FWI demonstrate better overall velocity fitting, further validating the efficacy of the method proposed in this paper.

For a simultaneous source seismic dataset, as shown in Fig. 27(a), seismic data from shots 161 to 168 were utilized. Fig. 27(b) illustrates the modeled seismic data using the initial velocity model (Fig. 21(a)), lacking reflection wave information

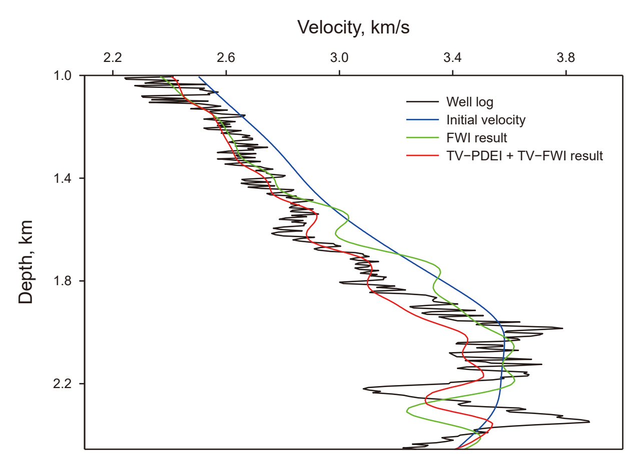

Fig. 26. A comparison between the well-log and inverted velocity for the SEG 2014 Chevron blind test dataset at 39.375 km.

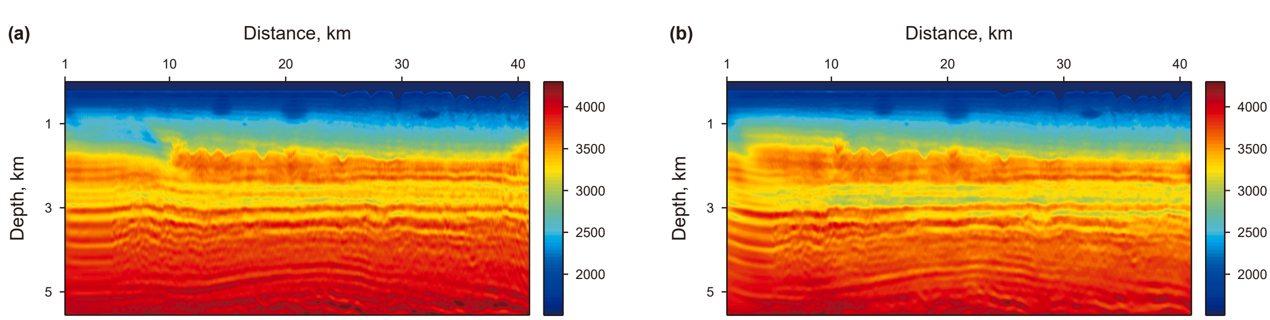

Fig. 25. High-frequency band (0–10 Hz) inversion results. **(a)** Multi-scale FWI using Fig. 24(a) as the initial model; **(b)** multi-scale TV-PDEI + Multi-scale TV-FWI (with weighting factor $\lambda_{TV} = 0.3$) using Fig. 24(c) as the initial model.

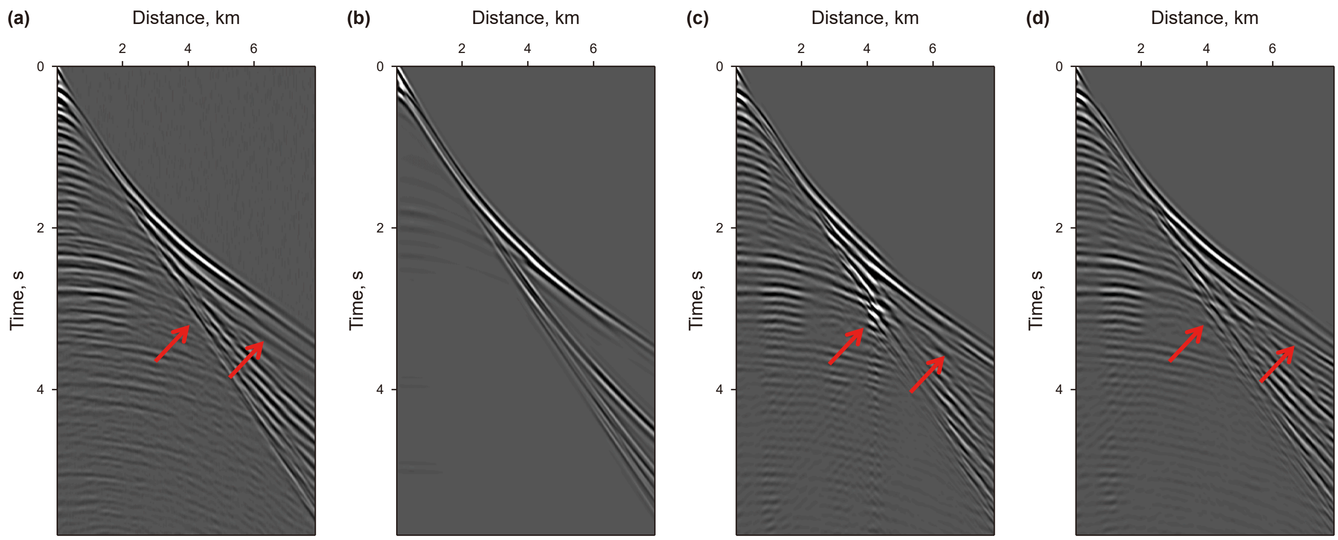

Fig. 27. Simultaneous source seismic data (0–10 Hz) from the SEG 2014 Chevron blind test dataset, consisting of 8 sources (shots 161–168): **(a)** observed data; **(b)** synthetic data using Fig. 21(a) as the velocity model; **(c)** synthetic data using Fig. 25(a) as the velocity model; **(d)** synthetic data using Fig. 25(b) as the velocity model.

due to the model's smoothness. Fig. 27(c) depicts seismic data modeled using the multi-scale FWI result (Fig. 25(a)), showing a good match between shallow reflections and observed data; however, the matching of refractions at far offsets and deep reflections requires improvement. Fig. 27(d) presents seismic data modeled using multi-scale TV-PDEI + multi-scale TV-FWI result (Fig. 25(b)), exhibiting excellent correspondence with observed data for both shallow reflection waves and refracted waves, further proving the accuracy of the velocity inversion results. Fig. 28 depicts the reverse time migration (RTM) images generated using the initial model (Fig. 21(a)) and the inverted models (Fig. 25). The comparison reveals that using the multi-scale TV-PDEI + multi-scale TV-FWI results (Fig. 25(b)) as the migration velocity model results in images with more continuous structures, particularly in areas indicated by the red arrows.

5. Discussion

This study demonstrates how the envelope and instantaneous phase information of a signal can be utilized to reconstruct the polarity envelope. The reconstructed polarity envelope not only includes ultra-low frequencies but also retains instantaneous phase information (Fig. 2). The choice of window length is crucial in determining the outcome of the polarity envelope reconstruction process. If a larger window is used, the reconstructed polarity envelope retrieves rich ultra-low frequency components, which is suitable for reconstructing the low wavenumber components of the velocity model. On the other hand, using a shorter window results in a polarity envelope that closely resembles the original waveform, typically containing more mid-frequency components, thus being more apt for reconstructing the mid-wavenumber components of the velocity model.

Based on the impact of window length on the low-frequency characteristics of the polarity envelope reconstruction, we can design a frequency-based multi-scale inversion strategy. Numerical tests have revealed that using the longest window, encompassing the envelope of an entire seismic event, can effectively reconstruct the missing ultra-low frequency components of seismic data. In our tests, we utilized a Gaussian window, which allows for a smoother truncation of seismic data. However, because the Gaussian window attenuates at both ends, increasing the length of the window could ensure capturing the waveform information of a seismic event completely. Thus, we chose the longest window to be four times the period length of the lowest frequency. Assuming seismic data lacks frequencies below 4 Hz, with the lowest frequency period being 1/4 s, the longest window used was 1 s. Of course, the choice of window length is not a strict parameter and can be longer to retrieve ultra-low wavenumber components of large-scale strong scattering structures. After setting the longest window, gradually decreasing the window length allows achieving the multi-scale PDEI method.

In implementing the PDEI method, computational resources consumption is predominantly attributed to the wave equation forward modeling and the calculation of polarity envelope. In implementing the 2D PDEI, the computation involves generating the polarity envelope of a 3D wavefield, which exhibits a computational cost comparable to that of the wave equation forward modeling. Fortunately, the calculation of the polarity envelope is independent of the model, allowing each time series to be computed separately. Additionally, the wave equation forward modeling between individual seismic shots is independent, enabling the use of CPU/GPU acceleration strategies to significantly enhance computational speed. Furthermore, employing a simultaneous source strategy, as elaborated in this study, can potentially boost the computation speed by more than eightfold, making the application feasible for 2D field data scenarios. However, in the realm of 3D FWI, which inherently demands substantial computational resources, the 3D PDEI algorithm necessitates computing the polarity envelope of a 4D wavefield. This challenge underscores the importance of creating faster methods to build polarity envelope in the future, helping to efficiently reduce the heavy computational demands.

Regarding the selection of total variation (TV) parameters, we implemented normalization parameters within the misfit function, making it relatively easier to choose regularization parameters. In numerical testing, we found that $\lambda_{\mathrm{TV}} = 0.6$ can effectively suppress inversion noise while preserving salt dome boundary. As seismic data's high-frequency components are integrated into the inversion process, reducing the value of λ_{TV} can help achieve higher resolution in velocity inversion results, avoiding overly smoothed outputs. For instance, in the blind data testing process, initial regularization parameter choice $\lambda_{\mathrm{TV}} = 0.6$ was made for TV-

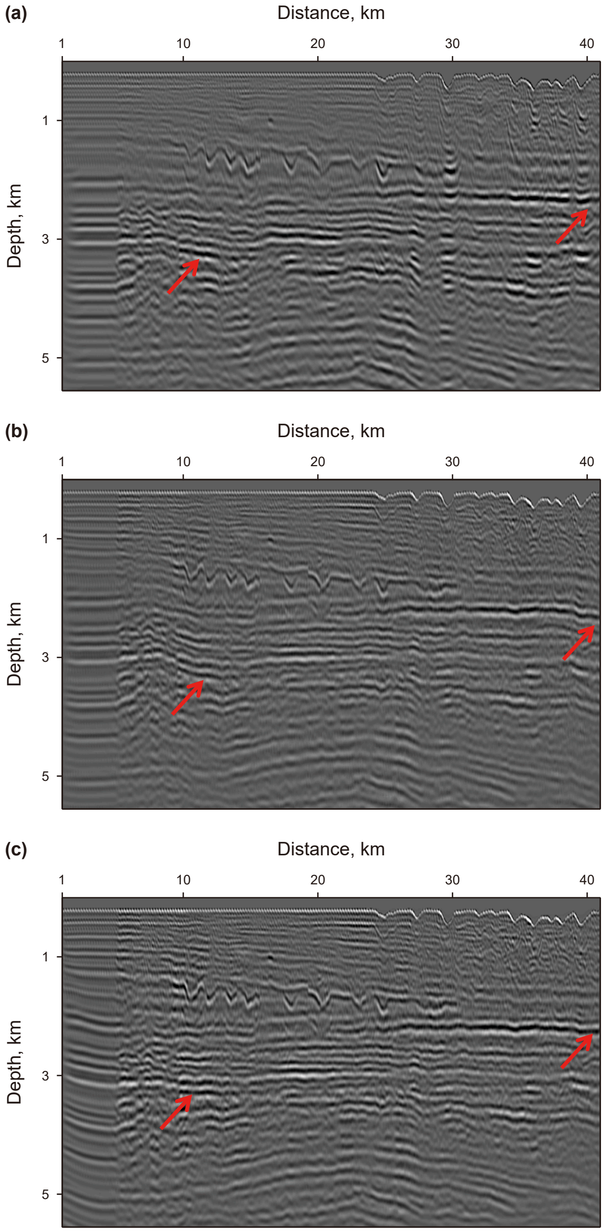

Fig. 28. RTM results: **(a)** RTM image using Fig. 21(a) as the migration velocity model; **(b)** RTM image using Fig. 25(a) as the migration velocity model; **(c)** RTM image using Fig. 25(b) as the migration velocity model.

PDEI method, and we gradually reduced it as more high-frequency components were introduced, continuing until it reached $\lambda_{TV} = 0.3$. This represents a multi-scale approach to regularization parameter selection, which is not strictly defined but rather determined by suitability.

Regarding the future development of envelope inversion methods, several key avenues are envisioned: (1) Developing novel envelope inversion theories and incorporating higher precision optimization algorithms to overcome the limitations of the Born approximation, thus achieving more stable and accurate inversion results; (2) Integrating envelope inversion with deep learning algorithms to transcend the inherent mapping relation between signals and velocity models, yielding more realistic velocity structure inversion results; (3) Combining envelope inversion with multi-physical field data to overcome the information barrier where only seismic envelope signals are used for velocity modeling, thus realizing multi-field joint inversion methods; (4) Applying envelope inversion to complex media and multi-component seismic data vector fields, such as elastic, visco-elastic, and anisotropic media. Additionally, fully utilizing multi-component seismic data vector fields can help discover vector characteristics of wavefields, thereby enhancing envelope inversion accuracy. By exploring these future research directions, envelope inversion can evolve to address the challenges posed by increasingly complex subsurface environments, thereby enriching the application of geophysical inversion methods.

6. Conclusions

To mitigate the influence of missing low-frequency information in seismic data on full waveform inversion (FWI) and efficiently obtain the low wavenumber components of large-scale, strong-contrast velocity structures, this study proposes a phase-based polarized direct envelope inversion with total variation regularization for simultaneous source seismic data (simultaneous source TV-PDEI) method. This method leverages the advantages of low-frequency envelopes and integrates instantaneous phase information with envelope signals to improve velocity inversion accuracy for the salt-bottom and subsalt structures. To enhance the computational efficiency and algorithm stability of the PDEI method, we employ a dynamic encoding strategy with simultaneous source and total variation regularization. This simultaneous source TV-PDEI method significantly boosts computational efficiency while mitigating crosstalk noise and maintaining inversion accuracy for salt structures. The testing results using single-shot and simultaneous source-based salt model and Chevron blind data tests indicate that the simultaneous source TV-PDEI provides a better initial velocity model for FWI with less computing resources, improving the velocity model inversion resolution of large-scale, strong-contrast salt velocity models.

CRediT authorship contribution statement

Yong Hu: Writing – review & editing, Writing – original draft, Software, Methodology, Funding acquisition, Data curation, Conceptualization. **Xi-Zhu Guan:** Investigation. **Li-Yun Fu:** Conceptualization. **Yi-Bo Wang:** Writing – review & editing, Resources. **Ru-Shan Wu:** Writing – review & editing, Methodology, Formal analysis.

Acknowledgments

This work is supported by the National Natural Science Foundation of China (Grant Nos. 42104116, 42230803).

Appendix A

According to scattering theory, in weak scattering media, the scattering wavefield can be represented as (Wu and Chen, 2017; Chen et al., 2018; Zhang et al., 2018; Hu et al., 2022):

$$\delta \mathbf{u} = \mathbf{G}_0 \mathbf{Q}_0 \, \delta \mathbf{v} \tag{A1}$$

where $\delta \mathbf{v}$ is the perturbation velocity, $\mathbf{G}_0$ is the background Green's operator and $\mathbf{Q}_0$ is the virtual source operator. In the time domain, the virtual source operator can be expressed as:

$$Q_0(\mathbf{x},\mathbf{x}',t)=\frac{2}{v_0^3(\mathbf{x}')}\frac{\partial^2}{\partial t^2}u_0(\mathbf{x}',t)\delta(\mathbf{x}-\mathbf{x}') \tag{A2}$$

However, in strong scattering media, seismic wave scattering primarily manifests as boundary reflections. According to the Kirchhoff integral, the scattered wavefield in strong scattering media can be expressed as (Wu and Chen, 2018):

$$\delta u(\mathbf{x}) = -\int_{\Gamma}\left\{u_s(\mathbf{x}_0)\frac{\partial}{\partial n}G_F(\mathbf{x};\mathbf{x}_0) - G_F(\mathbf{x};\mathbf{x}_0)\frac{\partial}{\partial n}u_s(\mathbf{x}_0)\right\}\mathrm{d}s(\mathbf{x}_0) \tag{A3}$$

where $\mathbf{G}_F = \mathbf{G}_0$. In strong scattering media, the scattering (reflection) intensity of seismic waves is proportional to the reflection coefficient. Thus, we can establish the relationship between the reflection coefficient and the scattered wavefield:

$$u_s(\mathbf{x}_0) = \gamma(\mathbf{x}_0,\vec{n})\, u_0(\mathbf{x}_0) = \gamma(\mathbf{x}_0,\vec{n})\, G_0(\mathbf{x}_0,\mathbf{x}_s) \tag{A4}$$

where $\mathbf{u}_0$ represents the seismic wavefield in the background medium, γ denotes the reflection coefficient, and $\vec{n}$ is the normal vector to the reflecting interface. Substituting Eq. (A4) into Eq. (A3), we obtain:

$$\delta u(\mathbf{x}_g) = -\left\{\int_{\Gamma}\gamma(\mathbf{x}_0,\vec{n})\left[G_F(\mathbf{x}_0;\mathbf{x}_s)\frac{\partial}{\partial n}G_F(\mathbf{x}_g;\mathbf{x}_0) - G_F(\mathbf{x}_g;\mathbf{x}_0)\frac{\partial}{\partial n}G_F(\mathbf{x}_0;\mathbf{x}_s)\right]\mathrm{d}s(\mathbf{x}_0)\right\} \tag{A5}$$

where $\mathbf{x}_0$ denotes the spatial location of the reflection interface, $\mathbf{x}_s$ is the source location, and $\mathbf{x}_g$ is the receiver location; $\mathrm{d}s(\mathbf{x}_0)$ is the boundary element at $\mathbf{x}_0$ on the boundary Γ. Under the assumption of small-angle scattering, the following relationship exists:

$$\frac{\partial}{\partial n}G_F(\mathbf{x}_g;\mathbf{x}_0) = -\frac{\partial}{\partial n}G_F(\mathbf{x}_0;\mathbf{x}_s), \frac{\partial}{\partial n}G_F(\mathbf{x}_0;\mathbf{x}_s) = G_F(\mathbf{x}_0;\mathbf{x}_s) \tag{A6}$$

Therefore, Eq. (A5) can be further simplified in its volume integral form to:

$$\delta u(\mathbf{x}_g,\mathbf{x}_s) = 2\int_V \gamma(\mathbf{x}_0,\vec{n})G_F(\mathbf{x}_g;\mathbf{x}_0)G_F(\mathbf{x}_0;\mathbf{x}_s)\,\mathrm{d}\mathbf{x}^3 \tag{A7}$$

In strong scattering media, we neglect the issue of seismic wave interference caused by thin layers, meaning each seismic wave packet contains a single seismic event without interference from another event. Thus, after squaring the above equation, the cross-term products inside the integral sign become zero. The scattering energy of the scattering wave can be approximately expressed as:

$$|\delta u\,(\mathbf{x}_g,\mathbf{x}_s)|^2 \approx 4\int_V \gamma^2(\mathbf{x}_0,\vec{n})|G_F(\mathbf{x}_g;\mathbf{x})|^2\,|G_F(\mathbf{x};\mathbf{x}_s)|^2\,\mathrm{d}\mathbf{x}^3 \tag{A8}$$

where γ is the reflection coefficient. For acoustic media, under the assumptions of constant density and small-angle scattering, the reflection coefficient can be approximately written as:

$$\gamma = \frac{v_2 - v_1}{v_2 + v_1} = \frac{\Delta v}{2v_0 + \Delta v} \tag{A9}$$

At the boundary between salt dome structures and the background medium, v_0 is the background velocity field, and $\Delta v = v_2 - v_1$ refers to the difference between the salt velocity and the background velocity.

Appendix B

In the time domain, based on the definition of signal energy, we can derive:

$$\int_0^{Tp}|\delta\mathbf{e}(t)|^2\mathrm{d}t = \int_0^{Tp}|\delta\mathbf{u}(t)|^2\mathrm{d}t \tag{B1}$$

where Tp is the time length for a seismic event, which also represents the time length for the energy packet of a seismic event, $\delta\mathbf{u}$ is the scattered wavefield, and $|\delta\mathbf{e}(t)|^2$ is the instantaneous energy of the scattering wave. When there is no interference between wavefields, the instantaneous energy of the scattering wave is approximately equivalent to the envelope of the scattering wave. As the seismic source wavelet approaches a unit impulse $\delta(\mathbf{x}-\mathbf{x}',t)$, the time length corresponding to the energy packet of a seismic event becomes $Tp\rightarrow 0$. Therefore, according to equation (B1), the instantaneous energy of the scattering wave and the absolute value of the scattering wave are related as follows:

$$|\delta\mathbf{e}(t)|^2 \approx |\delta\mathbf{u}(t)|^2 \tag{B2}$$

Of course, the aforementioned assumption $Tp\rightarrow 0$ is overly idealized, as real seismic events span a range of times. When the energy packet of a seismic event has a certain temporal length and each seismic trace contains multiple events, it can be represented using a sliding window function, defined by the following relationship:

$$\int_{t1}^{t2}|\delta\mathbf{e}(t)|^2\mathrm{d}t = \int_{t1}^{t2}|\delta\mathbf{u}(t)|^2\mathrm{d}t \tag{B3}$$

where $t1, t2$ indicates the start and end times of the sliding window function. Therefore, within a sequence of finite temporal length, Eq. (B3) effectively applies a smoothing or low-pass filtering operation to both $|\delta\mathbf{e}(t)|^2$ and $|\delta\mathbf{u}(t)|^2$.This enables us to better demonstrate the correctness of the assertion that the smoothed energy of the scattering wave and the smoothed absolute value of the scattering wave are equivalent (Bharadwaj et al., 2016). By substituting Eq. (A8) into Eq. (B2), we obtain:

$$|\delta\mathbf{e}(t)|^2 \approx |\delta\mathbf{u}(t)|^2 = 4\,|\mathbf{G}_F|^2\,|\mathbf{G}_F|^2\,\gamma^2 \tag{B4}$$

Substituting Eq. (A9) into Eq. (B4), we get:

$$|\delta\mathbf{e}(t)|^2 \approx |\delta\mathbf{u}(t)|^2 = |\mathbf{G}_F|^2\,|\mathbf{Q}_\gamma|^2\,\delta\mathbf{v}^2 \tag{B5}$$

The corresponding time domain virtual source operator $\mathbf{Q}_\gamma$ can be expressed as:

$$|Q_\gamma(\mathbf{x},\mathbf{x}',t)|^2 = \frac{4}{(2\mathbf{v}_0+\Delta\mathbf{v})^2}|G_F(\mathbf{x}',t,\mathbf{x}_s)|^2\delta(\mathbf{x}-\mathbf{x}') \tag{B6}$$

In gradient-based inversion methods such as the quasi Gauss-Newton method, the step length is typically chosen to be small. For the Nth update step, we define:

$$\Delta\mathbf{v} = N\xi_v \tag{B7}$$

where N represents the iteration number, and ξ_v is the velocity update at each step. Therefore $2\mathbf{v}_0 \gg \xi_v$. For each step of the velocity update, the virtual source can be expressed as (Wu and Chen, 2017; Chen et al., 2018; Zhang et al., 2018; Hu et al., 2022):

$$\left|Q_{\gamma}(\mathbf{x},\mathbf{x}',t)\right| = \frac{1}{\mathbf{v}_0}\left|G_F(\mathbf{x}',t,\mathbf{x_s})\right|\delta(\mathbf{x}-\mathbf{x}'). \tag{B8}$$

When there is no interference between wavefields, the instantaneous energy of the scattering wave can be approximated as equal to the envelope of the scattering wave. We can represent the perturbation of the envelope as:

$$|\delta\mathbf{e}| = \mathbf{G}_\mathrm{E}\,\mathbf{Q}_\mathrm{E}\,\delta\mathbf{v} \tag{B9}$$

where $\mathbf{G}_\mathrm{E} = |\mathbf{G}_\mathrm{F}|$, $\mathbf{Q}_\mathrm{E} = |\mathbf{Q}_\gamma|$.

Appendix C

The DEI misfit function can be expressed as:

$$J_\mathrm{E}(\mathbf{v}) = \frac{1}{2}\sum_{Ns}\sum_{Nt}\sum_{Nr}\left[E_\mathrm{u}(t) - E_\mathrm{d}(t)\right]^2 \tag{C1}$$

The gradient of the envelope misfit can be written as,

$$\frac{\partial J_\mathrm{E}(\mathbf{v})}{\partial\mathbf{v}} = \sum_{Ns}\sum_{Nt}\frac{\partial(E_\mathrm{u})}{\partial\mathbf{v}}\quad(E_\mathrm{u} - E_\mathrm{d}). \tag{C2}$$

where $\mathbf{F}_\mathrm{E} = \partial E_u/\partial\mathbf{v}$ is the Fréchet derivative of the direct envelope (Wu and Chen, 2017; Chen et al., 2018; Zhang et al., 2018; Hu et al., 2022).

$$\frac{\partial J_\mathrm{E}(\mathbf{v})}{\partial\mathbf{v}} = (\mathbf{F}_\mathrm{E})^\mathrm{T} f_s^\mathrm{DEI} \tag{C3}$$

where T is matrix transpose; $f_s^\mathrm{DEI} = E_\mathrm{u} - E_\mathrm{d}$ is the DEI adjoint source. $\mathbf{F}_\mathrm{E}$ is the direct envelope Fréchet derivative, which has the following relationship with the Green's function and virtual source operator:

$$\mathbf{F}_\mathrm{E} = \mathbf{G}_\mathrm{E}\mathbf{Q}_\mathrm{E} \tag{C4}$$

where $\mathbf{G}_\mathrm{E}$ is the envelope (or smoothed amplitude) Green function and $\mathbf{Q}_\mathrm{E}$ is the DEI virtual source operator. By substituting the above equations into Eq. (C1), the gradient of DEI is finally expressed as:

$$\frac{\partial J_\mathrm{E}(\mathbf{v})}{\partial\mathbf{v}} = \frac{1}{\mathbf{v}_0}\sum_{Ns}\sum_{Nt}\left(P_\mathrm{f}^\mathrm{E}\right)\left(P_\mathrm{b}^\mathrm{E}\right) \tag{C5}$$

where P_f^E is the envelope of the forward-propagated wavefield, and P_b^E is the back-propagated wavefield of energy (envelope or smoothed amplitude) residual.

References

Almomin, A., Biondi, B., 2015. Generalization and amplitude normalization of tomographic full waveform inversion. In: SEG Technical Program Expanded Abstracts 2015, pp. 1309–1313. https://doi.org/10.1190/segam2015-5919588.1.

Ao, R.D., Dong, L.G., Chi, B.X., 2015. Source-independent envelope-based FWI to build an initial model. Chin. J. Geophys. 58 (6), 1998–2010. https://doi.org/10.6038/cjg20150615 (in Chinese).

Burstedde, C., Ghattas, O., 2009. Algorithmic strategies for full waveform inversion: 1D experiments. Geophysics 74 (6), WCC37–WCC46. https://doi.org/10.1190/1.3237116.

Bozdağ, E., Trampert, J., Tromp, J., 2011. Misfit functions for full waveform inversion based on instantaneous phase and envelope measurements. Geophys. J. Int. 185 (2), 845–870. https://doi.org/10.1111/j.1365-246X.2011.04970.x.

Bharadwaj, P., Mulder, W., Drijkoningen, G., 2016. Full waveform inversion with an auxiliary bump functional. Geophys. J. Int. 206 (2), 1076–1092. https://doi.org/10.1093/gji/ggw129.

Chi, B., Dong, L., Liu, Y., 2014. Full waveform inversion method using envelope objective function without low frequency data. J. Appl. Geophys. 109, 36–46. https://doi.org/10.1016/j.jappgeo.2014.07.010.

Chen, G.X., Wu, R.S., Chen, S.C., 2018. Reflection multi-scale envelope inversion. Geophys. Prospect. 66 (7), 1258–1271. https://doi.org/10.1111/1365-2478.12624.

Feng, D., Cao, C., Wang, X., 2019. Multiscale full-waveform dual-parameter inversion based on total variation regularization to on-ground GPR data. IEEE Trans. Geosci. Rem. Sens. 57 (11), 9450–9465. https://doi.org/10.1109/TGRS.2019.2926626.

Fichtner, A., Kennett, B.L.N., Igel, H., et al., 2008. Theoretical background for continental- and global-scale full-waveform inversion in the time–frequency domain. Geophys. J. Int. 175 (2), 665–685. https://doi.org/10.1111/j.1365-246X.2008.03923.x.

Fu, H., Zhang, Y., Li, X., 2021. Adaptive overcomplete dictionary learning-based sparsity-promoting regularization for full-waveform inversion. Pure Appl. Geophys. 178, 411–422. https://doi.org/10.1007/s00024-021-02662-w.

Hu, Y., Han, L.G., Xu, Z., et al., 2017. Demodulation envelope multi-scale full waveform inversion based on precise seismic source function. Chin. J. Geophys. 60 (3), 1088–1105. https://doi.org/10.6038/cjg20170321 (in Chinese).

Hu, Y., Wu, R.S., Han, L.G., et al., 2019. Joint multiscale direct envelope inversion of phase and amplitude in the time–frequency domain. IEEE Trans. Geosci. Rem. Sens. 57 (7), 5108–5120. https://doi.org/10.1109/TGRS.2019.2896936.

Hu, Y., Wu, R.S., Huang, X., et al., 2022. Phase-amplitude-based polarized direct envelope inversion in the time-frequency domain. Geophysics 87 (3), R245–R260. https://doi.org/10.1190/geo2020-0956.1.

Kalita, M., Kazei, V., Choi, Y., et al., 2019. Regularized full-waveform inversion with automated salt flooding. Geophysics 84 (4), R569–R582. https://doi.org/10.1190/geo2018-0146.1.

Kadu, A., van Leeuwen, T., Mulder, W.A., 2016. Salt reconstruction in full-waveform inversion with a parametric level-set method. IEEE Trans. Comput. Imag. 3 (2), 305–315. https://doi.org/10.1109/TCI.2016.2640761.

Lailly, P., 1983. The seismic inverse problem as a sequence of before stack migrations. In: Conference on Inverse Scattering, Theory and Applications. Society for Industrial and Applied Mathematics, Philadelphia, pp. 206–220.

Lee, D., Kang, S.G., Kim, S., et al., 2024. Efficient direct envelope inversion with excitation amplitude for strong velocity contrast model. IEEE Trans. Geosci. Rem. Sens. 62, 1–12. https://doi.org/10.1109/TGRS.2024.3422978.

Li, X., Aravkin, A.Y., van Leeuwen, T., et al., 2012. Fast randomized full-waveform inversion with compressive sensing. Geophysics 77 (3), A13–A17. https://doi.org/10.1190/geo2011-0410.1.

Luo, J., Wu, R.S., 2015. Seismic envelope inversion: reduction of local minima and noise resistance. Geophys. Prospect. 63 (3), 597–614. https://doi.org/10.1111/1365-2478.12208.

Métivier, L., Brossier, R., Mérigot, Q., et al., 2016. Measuring the misfit between seismograms using an optimal transport distance: Application to full waveform inversion. Geophys. J. Int. 205, 345–377. https://doi.org/10.1093/gji/ggw014.

Ramirez, C., Larrazabal, G., González, G., et al., 2016. Salt body detection from seismic data via sparse representation. Geophys. Prospect. 64 (2), 335–347. https://doi.org/10.1111/1365-2478.12261.

Sun, B., Alkhalifah, T., 2019. Robust full-waveform inversion with Radon-domain matching filter. Geophysics 84 (5), R707–R724. https://doi.org/10.1190/geo2018-0347.1.

Song, C., Feng, X., Gao, Y., et al., 2024. Elastic wavefield reconstruction inversion with source estimation. IEEE Trans. Geosci. Rem. Sens. 62, 1–9. https://doi.org/10.1109/TGRS.2023.3339513.

Tarantola, A., 1984. Inversion of seismic reflection data in the acoustic approximation. Geophysics 49 (8), 1259–1266. https://doi.org/10.1190/1.1441754.

Tikhonov, A.N., Arsenin, V.Y., 1977. Solutions of Ill-Posed Problems. Wiley, New York, p. 30.

Vigh, D., Jiao, K., Cheng, X., et al., 2016. Earth-model building from shallow to deep with full-waveform inversion. Lead. Edge 35, 1025–1030. https://doi.org/10.1190/tle35121025.1.

Warner, M., Guasch, L., 2015. Robust adaptive waveform inversion. In: SEG Technical Program Expanded Abstracts 2015, pp. 1059–1063. https://doi.org/10.1190/segam2015-5853026.1.

Wang, Y., Wu, R.S., Chen, G., et al., 2018. Seismic modulation model and envelope inversion with smoothed apparent polarity. J. Geophys. Eng. 15 (5), 2278–2286. https://doi.org/10.1088/1742-2140/aac54d.

Wu, R.S., Luo, J., Wu, B., 2014. Seismic envelope inversion and modulation signal model. Geophysics 79 (3), WA13–WA24. https://doi.org/10.1190/geo2013-0294.1.

Wu, R.S., Chen, G., 2017. New Fréchet derivative for envelope data and multi-scale envelope inversion. In: 79th EAGE Conference and Exhibition 2017. https://doi.org/10.3997/2214-4609.201700833.

Wu, R.-S., Chen, G., 2018. Multi-scale seismic envelope inversion using a direct envelope Fréchet derivative for strong-nonlinear full waveform inversion. arXiv:1808.05275. https://doi.org/10.48550/arXiv.1808.05275.

Yong, P., Liao, W., Huang, J.P., et al., 2018. Total variation regularization for seismic waveform inversion using an adaptive primal dual hybrid gradient method. Inverse Probl. 34 (4), 045006. https://doi.org/10.1088/1361-6420/aaaf8e.

Yong, P., Liao, W., Huang, J.P., et al., 2019. Misfit function for full waveform inversion based on the Wasserstein metric with dynamic formulation. J. Comput. Phys. 399, 108911. https://doi.org/10.1016/j.jcp.2019.108911.
Yong, P., Brossier, R., Métivier, L., et al., 2023. Localized adaptive waveform inversion: Theory and numerical verification. Geophys. J. Int. 233 (2), 1055–1080. https://doi.org/10.1093/gji/ggac496.
Yang, F., Ma, J., 2023. FWIGAN: Full-waveform inversion via a physics-informed generative adversarial network. J. Geophys. Res. Solid Earth 128 (4), e2022JB025493. https://doi.org/10.1029/2022JB025493.
Zhang, P., Wu, R.S., Han, L., 2018. Source-independent seismic envelope inversion based on the direct envelope Fréchet derivative. Geophysics 83 (6), R581–R595. https://doi.org/10.1190/geo2017-0360.1.
Zhu, L., Liu, E., McClellan, J.H., 2015. Sparse-promoting full waveform inversion based on online orthonormal dictionary learning. Geophysics 82 (2), R87–R107. https://doi.org/10.1190/geo2014-0577.1.